Snow Mapping from Passive Microwave Brightness Temperature and MODIS Snow Product with Machine learning Approaches

by

Jiayi Du

A thesis

presented to the University of Waterloo

in fulfillment of the

thesis requirement for the degree of

Master of Science

in

Geography

Waterloo, Ontario, Canada, 2023

Author's declaration

I hereby declare that I am the sole author of this thesis. This is a true copy of the thesis, including any required final revisions, as accepted by my examiners.

I understand that my thesis may be made electronically available to the public.

Abstract

Snow cover is one of the cryosphere's most critical components, representing a vital geophysical variable for climate and hydrology. Monitoring snow cover in Arctic regions has gained increasing significance, particularly considering recent climate warming. Given the complex spatiotemporal variability, inconvenience of transportation, and the remote locations of many snow-covered areas, remote sensing emerges as an ideal technique for data collection to monitor snow cover across various spatiotemporal scales.

In contrast to optical remote sensing, passive microwave (PMW) and active microwave (AMW) satellite sensors remain unaffected by clouds and solar illumination, making them widely employed in snow detection. PMW observations have lower spatial resolution and high temporal resolution than AMW, which are suitable for large-scale snow mapping. Integrating optical data and PMW data can significantly enhance the quality of snow cover information. Various machine learning (ML) methods have been pivotal in environmental remote-sensing research in recent years. With the surge in Earth observation big data and the rapid advancements in ML techniques, an array of innovative methods has emerged to facilitate environmental monitoring on a global scale. Thus, a snow-monitoring method has been proposed based on multi-source remote sensing data and ML. The brightness temperature (Tb) data derived from the Advanced Microwave Scanning Radiometer E/2 (AMSR-E/2) Level 3 product and Moderate Resolution Imaging Spectroradiometer (MODIS) snow product serves as the reference for snow cover area (SCA). This study predominantly selects Oct, Dec, Feb, and Apr from 2012 to 2022 as the study periods. The research uses three ML methods, Logistic Regression (LR), Random Forest (RF) and Support Vector Machine (SVM), for snow cover detection based on PMW and MODIS data in the Arctic. The overall accuracy (The ratio of correctly classified as snow plus correctly classified as non-snow points to the total number of points) of ML models in snow detection surpasses 80%, yet it exhibits regional and seasonal variations. Notably, distinctions in the distribution of MODIS snow and PMW snow become evident in two types of areas: regions where MODIS estimates exceed PMW and those where PMW

estimates surpass MODIS. ML-based estimation significantly enhances the accuracy of snow monitoring in the latter category, reducing misclassifications and augmenting the precision of snow cover assessment. When comparing the ML-derived SCA, PMW-derived SCA, and MODIS-derived SCA with the snow depth dataset-derived SCA, the ML method exhibited the highest consistency.

Acknowledgements

I wish to extend my deepest appreciation to my thesis supervisor, Dr. Richard Kelly. Your exceptional mentorship, unwavering support, and boundless wisdom have been the cornerstone of this thesis. Your guidance has not only enriched my academic journey but has also set a remarkable standard for excellence that I will carry forward with me.

I would like to acknowledge the contributions of the other esteemed members in our research group: Alex, Lina, Aaron, Akash, Jeffery, Margot, Vicky, Wei, Qinghuan and Zeinab. Your collaborative efforts, thought-provoking discussions, and shared experiences have been invaluable in shaping the research and my academic growth.

To my husband Alex, your enduring encouragement, patience, and belief in me have been my constant motivation. Your steadfast support throughout this endeavor has meant the world to me, and I am profoundly grateful for your unwavering presence by my side.

I extend my heartfelt thanks to the members of the defense committee Dr. Fraser King and Dr. Grant Gunn for their expertise, time, and insightful evaluations that have elevated the quality of this thesis.

To my family and friends, your encouragement and faith in me have been a driving force in reaching this milestone.

To all those who have been part of this remarkable journey, your contributions have made it possible for me to complete this master's thesis.

Table of Contents

List of Figures

List of Tables

List of Abbreviations

AUC - Area Under the Curve

AMW - Active Microwave

AMSR-E/2 - Advanced Microwave Scanning Radiometer E/2

ASTER - Advanced Spaceborne Thermal Emission Reflection Radiometer

CGF - Cloud Gap Filling

CMC - Canadian Meteorological Centre

CMC-SCA - Canadian Meteorological Centre Snow Cover Area

DMRT - Dense Medium Radiative Transfer

DMSP - Defense Meteorological Satellites Program

EASE - Equal-Area Scalable Earth

FSC - Fractional Snow Cover

FP - False Positive

FN - False Negative

GLWD - Global Lake and Wetland Database

GCOM-W1 - Global Change Observation Mission-Water

GEM - Global Environmental Multiscale

HUT - University of Helsinki

IPCC - Intergovernmental Panel on Climate Change

LR - Logistic Regression

MSE - Mean Squared Error

ML - Machine Learning

ML-SCA – Machine Learning Derived Snow Cover Area

MLC - Maximum Likelihood Method

MODIS - Moderate Resolution Imaging Spectroradiometer

MODIS-SCA - MODIS derived Snow Cover Area

MWRI - Microwave Radiation Imager

NDSI - Normalized Differential Snow Index

NSIDC - National Snow and Ice Data Center

OA - Overall Accuracy

PF - Polarization Fraction

PMW - Passive Microwave

PMW-SCA - Passive Microwave Derived Snow Cover Area

POM - Passive Microwave Overestimated than MODIS

PUM - Passive Microwave Underestimated than MODIS

QSCAT - Quick Scatterometer

RF - Random Forest

RF-SCA - Random Forest Derived Snow Cover Area

ROC - Receiver Operating Characteristic Curve

RBF - Radial Basis Function

SAR - Synthetic Aperture Radar

SCA - Snow Cover Area

SD - Snow Depth

SMMR - Scanning Multichannel Microwave Radiometer

SAR - Synthetic Aperture Radar

SSM/I - Special Sensor Microwave Imager

SSMIS - Special Sensor Microwave Imager Sounder

SVM - Support Vector Machine

SWE - Snow Water Equivalent

SWIR - Shortwave Infrared Red

TA - Antenna Temperature

Tb - Brightness Temperature

TP - True Positive

TN - True Negative

VCF - Vegetation Continuous Field

WSI - Water-Resistant Snow Index

Chapter 1
Introduction

1.1 The importance of snow

As outlined in the Intergovernmental Panel on Climate Change's (IPCC) Sixth Assessment Report for 2021 (AR6), substantial changes are evident in the cryosphere due to ongoing global warming. These transformations, including the Arctic amplification phenomenon, are anticipated to persist, influencing both human and physical dimensions (Callaghan et al., 2011b). These changes in the cryosphere hold the potential for severe consequences in many mountainous areas, such as flooding, landslides, and impacts on water availability, affecting humans, infrastructure, and economies (Beniston, 2003). Snow cover, a vital element of the cryosphere, exhibits wide distribution, strong seasonality, and heightened sensitivity to weather and climate fluctuations within Earth's climate system (Thackeray et al., 2019). It serves as a significant feedback mechanism within the global climate system (Callaghan et al., 2011b; Derksen et al., 2012; Cohen et al., 2012). Moreover, snow cover plays a crucial role in groundwater and river runoff. When combined with melting glaciers, it can contribute to the occurrence of natural disasters such as avalanches, rain, and snow-induced flooding. Additionally, snow is instrumental in maintaining mountain forests and Arctic ecosystems. Its impact extends to Earth's energy budget by reflecting solar radiation (known as the snow-albedo effect) and influencing permafrost temperatures (Abram et al., 2019). Thus, ensuring precise monitoring of snow distribution is a fundamental prerequisite for examining pressing issues, including global climate change, hydrological cycles, human well-being, and economic stability.

1.1.1 Global climate change

As a crucial component of the cryosphere, snow cover ranks among the most responsive elements to climate change. Research has established that, within the context of global warming, the pivotal factor driving accelerated polar warming in polar regions is the positive feedback process (Masson-Delmotte et al., 2006). This feedback process encompasses several

mechanisms, with the snow albedo feedback being of particular significance (Screen & Simmonds, 2010).

Snow albedo represents the ratio of solar radiation reflected by the snow surface to the total solar radiation received by it. While a blackbody has an albedo of 0 because it predominantly absorbs visible light, fresh snow exhibits a high albedo, reflecting more than 80% of the incoming solar radiation (Dobos, 2020). As illustrated in Figure 1.1, the concept of snow albedo feedback involves an initial disturbance, such as an increase in greenhouse gases, leading to elevated surface temperatures, snowmelt, and a reduction in snow coverage. Consequently, surface albedo decreases as the snow cover diminishes. This decline results in increased absorption of solar radiation by the Earth's surface, further intensifying surface warming and exacerbating snowmelt (Thackeray & Fletcher, 2016).

It is worth noting that surface albedo decreases by approximately 1% per degree of warming (Fletcher et al., 2012). In higher latitudes, the impact of snow albedo feedback is particularly noticeable during spring and could contribute to the declining trend in snow cover extent. The evolving surface air temperatures and shifts in precipitation patterns may further influence the trend in snow cover extent, contingent on factors such as latitude and elevation (Hernandez-Henriquez et al., 2015).

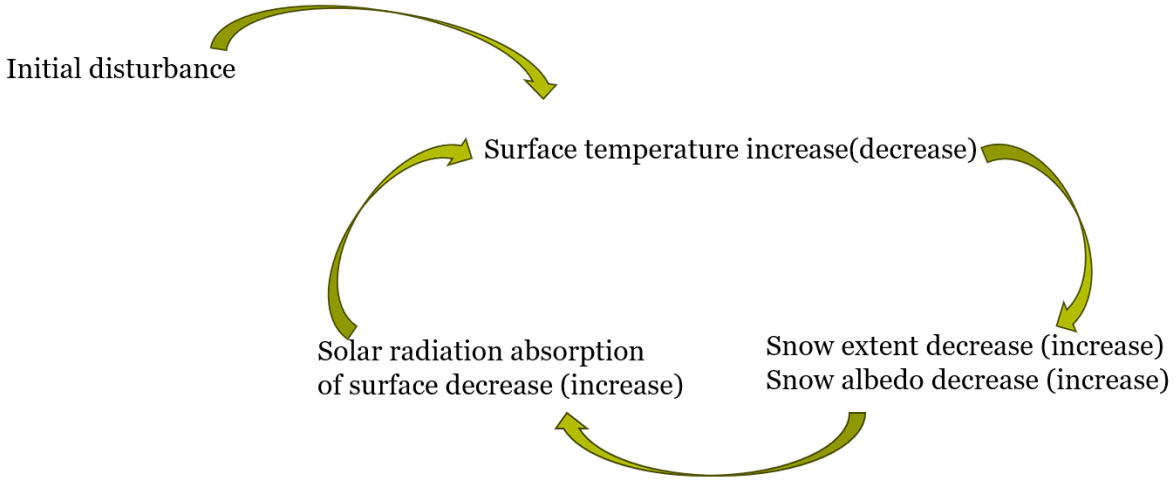

Figure 1. 1 The feedback mechanism of snow albedo

1.1.2 Hydrological cycles

In the context of global climate change, the diminished snowmelt, influenced by climate change, reduces the availability of frozen water resources by disrupting the natural replenishment of downstream water sources. This increasing meltwater gradually reshapes hydrological processes, exerting a profound influence on the hydrological function of snow cover. This influence primarily manifests in water conservation, runoff recharge, and water resource regulation (Ding et al., 2020). Snow acts as a vital component in the phase-change process, resembling a sitting water tower that facilitates the conversion of solid water into liquid water, releasing previously stored water. Consequently, snow continues to provide water even during periods of drought and low rainfall. Snowmelt events lead to the loss of snow water storage and advance the spring snow-free date. Furthermore, a transition towards increased winter rainfall can reduce overall river runoff (Berghuijs et al., 2014). In the Arctic, snowmelt runoff accounts for a substantial 65% of the annual runoff (Shi et al., 2015). The melting of snow also profoundly impacts frozen soil ecosystems, which serve a critical role in water conservation. These ecosystems are instrumental in stabilizing the water cycle and river runoff in the source regions of rivers. Compared to snow's water conservation and runoff recharge functions, its role in water resource regulation is of paramount importance. In basins without snow cover, rivers depend on precipitation for replenishment, resulting in significant annual runoff variations. In contrast, within snow-covered basins, the temperature in high mountain snow areas often remains lower due to increased precipitation during wet years. The reduced volume of glacier melting also diminishes the supply of snowmelt water to the rivers, weakening the increased watershed runoff resulting from augmented precipitation. Conversely, in basins with low precipitation, the relatively higher temperatures in glacier areas lead to increased glacial meltwater, compensating for river replenishment due to insufficient precipitation (Ding et al., 2020).

1.1.3 Human welfare

Approximately 100 million people depend on snowmelt water for their agricultural and domestic needs, as documented by Barnett et al. in 2005. Additionally, nearly the entire global

population benefits from the climate-related services provided by snow, as a significant portion of the world's annual precipitation comes in the form of snowfall (Sturm et al., 2017). In regions with high latitudes and altitudes, where the active layer of frozen soil remains intact, snowmelt often gives rise to floods and disasters, impacting both the social economy and human safety. Changes in winter precipitation and runoff patterns, leading to the loss of snow water, result in significant economic setbacks for areas reliant on snowmelt in industrial agriculture. The importance of snow in human life may not be fully recognized by those who live far from regions where snow is directly supplied. To convey the significance of snow to human economic well-being, Sturm et al. (2017) have made efforts to monetize its value. Taking the western United States as an example, the transition from snow to rain would result in annual losses ranging from $10.8 billion to $48.6 billion.

1.2 The methods of snow detection

1.2.1 In situ measurement

The simplest method for snow detection involves using equipment to collect in-situ measurements. These devices are primarily categorized into two types: fixed and portable. Snow monitoring heavily relies on observational data from operational weather stations distributed across a wide area, serving the purpose of continuous monitoring to record the evolution of snow cover (Kinar & Pomeroy, 2015). In contrast, portable equipment is tailored to small-scale areas, requiring manual transportation of measuring devices into snowy terrain for data collection. Common equipment used for measuring snow depth and snow water equivalent includes rulers and snow tubes. For example, the Magnaprobe, a patented automatic snow depth probe commercially manufactured by Snow-Hydro LLC since 1999, has found extensive use in field validation campaigns. Its design includes a ski pole-like rod housing a magneto strictive device, accompanied by a floating basket and magnet assembly (Sturm & Holmgren, 2018). When measuring snow wetness or dielectric constant, electronic equipment is necessary for accurate assessment (Kinar & Pomeroy, 2015).

1.2.2 Remote sensing observations

Due to the remoteness of some areas, weather station observations are limited in their representation of the region. Remote sensing technology provides a rapid, efficient, and extensive means of monitoring snow-covered area (SCA), snow depth, and other snow-related parameters. Currently, remote sensing methods employed for snow monitoring are primarily based on optical and microwave technologies, with microwave remote sensing further categorized into active microwave remote sensing (AMW) and PMW.

1.2.2.1 Optical remote sensing

Optical remote sensing data, from visible-infrared observations, are typically employed for estimating SCA, with the Normalized Differential Snow Cover Index (NDSI) serving as the primary tool for snow cover identification (Hall et al., 2002). Identifying snow in multispectral data relies on variations in snow reflectance across different spectral bands. Snow exhibits high reflectance in the visible spectrum and low reflectance in the short-wave infrared. NDSI, being a globally applicable algorithm, effectively facilitates snow mapping based on these characteristics. Other snow indices are also employed for snow cover measurement. For instance, Sharma et al. (2016) introduced the Water-Resistant Snow Index (WSI) for snow cover mapping, excluding water bodies. Alternatively, the relationship between NDSI and Fractional Snow Cover (FSC) is established using an empirical function (Gascoin et al., 2020). When it comes to data usage, the fusion of multi-source data has proven to be an effective approach for enhancing the accuracy of snow mapping. For example, Gascoin et al. (2019) developed a high-resolution SCA model based on Sentinel 2 and Landsat 8 data.

Currently, optical remote sensing sensors are primarily employed for remote sensing monitoring of snow cover area and snow reflectance. However, they are less effective in estimating snow depth, snow water equivalent, and other related parameters due to the characteristics of snow and the limitations of optical wavelengths. Furthermore, optical remote sensing is susceptible to weather conditions, and cloud cover can significantly impact monitoring efforts.

1.2.2.2 Microwave remote sensing

Compared to optical remote sensing, microwave remote sensing has proven to be a highly effective technique for monitoring and obtaining snow parameters. Microwaves can penetrate clouds and snow layers, allowing the detection of information about the surface beneath the snow cover. This technology is characterized by its all-weather capabilities and large-scale snow cover monitoring (Shi et al., 2016).

AMW and PMW remote sensing methods effectively retrieve snow depth and snow water equivalent, offering advantages that optical remote sensing cannot match. The era of snow monitoring using AMW sensor data began with the launch of the first synthetic aperture radar (SAR) satellite, SeaSat, in 1978 (Pepe et al., 2005). SAR primarily relies on the backscattering coefficient, co-polarization and cross-polarization backscattering ratios, and polarization fraction (PF) values to distinguish between snow cover and non-snow cover areas (Singh et al., 2014). For example, Shi et al. (2000) utilized the co-polarization channels of multi-frequency L-band and C-band SAR data to achieve high-precision inversion in snow-covered areas. Additionally, backscatter information can be combined with interference coherence to enhance snow identification accuracy (Strozzi et al., 1999).

In contrast to AMW, PMW snow detection relies on the Tb value. Most PMW-based snow monitoring algorithms utilize decision tree classification methods. The primary criterion for identifying snow cover is the positive Tb gradient between low and high frequencies (e.g. 18GHz and 36GHz) (Shi et al., 2016). Kunzi et al. (1982) mapped SCA by applying the condition 18GHz-37GHz > 3.8K. Grody and Basist (1996) introduced a decision tree algorithm based on snow cover measurements from the SSM/I, separating snow from precipitation, cold deserts, and frozen ground. Some algorithms identify SCA with different types of snow. Kelly (2009) developed a shallow snow detection algorithm using an 89 GHz channel to distinguish moderate to deep snow.

However, the coarse resolution (e.g. 25km) of PMW remote sensing data introduces the issue of mixed pixels, potentially containing complex terrain or multiple land types. This may lead to inaccuracies when retrieving snow parameters based on PMW remote sensing

(Foster et al., 1997). The coarse spatial resolution of PMW remote sensing data will bring about the problem of mixed pixels (may contain complex terrain or multiple land types), which leads to the failure to accurately describe the real snow information on the surface when retrieving snow parameters based on PMW remote sensing (Foster et al., 1997).

1.2.3 Artificial intelligence technique in snow detection

Utilizing a linear empirical relationship for snow parameter calculation offers advantages such as simplicity, interpretability, computational efficiency, and stability. However, studies have shown that the relationship between microwave brightness temperature and snow cover parameters becomes complex and nonlinear, exhibiting a many-to-many functional relationship across diverse terrains (e.g., Liang et al., 2015). Consequently, developing an explicit inverse relationship for snow cover parameters is deemed unrealistic. To enhance the accuracy of estimating snow cover parameters, it becomes necessary to employ nonlinear techniques, such as Neural Networks (NNs), SVM, RF, and other ML algorithms (Gharaei-Manesh et al., 2016). These nonlinear methods have proven successful in the inverse estimation of snow depth and snow water equivalent to date (Kwon et al., 2019; Xiao et al., 2018; Liang et al., 2015). Nonlinear inversion algorithms, built on prior knowledge, effectively capture the intricate relationship between microwave brightness parameters and snow cover, overcoming the limitations of linear algorithms when applied across various regions. Despite their widespread use and high inversion accuracy, these algorithms lack the detailed snow physical model processes found in the inversion process (Xue & Forman, 2015).

1.3 Aim and Objectives

Given the significance of large-scale snow mapping, the limitations of traditional remote sensing methods, and the relatively limited application of ML in snow classification, this study aims to assess the suitability of ML approaches for snow mapping in the Arctic using PMW Tb data and MODIS observations. To achieve this overarching goal, the following objectives are defined:

1. Evaluate various ML models for snow detection.

Utilizing PMW Tb data and MODIS binary snow data as inputs, three commonly employed ML models, LR, RF and SVM classifiers, are assessed. The optimal models are determined through hyperparameter tuning and cross-validation. Subsequently, their effectiveness is examined on an evaluation dataset.

2. Analyze the disparities between satellite-derived snow, ML-derived snow which combines optical and PMW observations, and station-measured snow.

   Satellite-derived snow encompasses data from both PMW and MODIS sources, with the expectation that ML-derived snow exhibits improved consistency with MODIS snow data. These variations can be analyzed from multiple perspectives, including Tb features, topographic characteristics, and detection algorithms. Furthermore, station-derived snow cover data can serve as a reference for comparing estimated snow data from ML, considering the differences in data sources and algorithms.

1.4 Thesis structure

Chapter 2 provides the background information of this research, which includes an introduction to the basis theory of snow detection and a review of the use of PWM, MODIS, and ML applications for snow cover detection. In Chapter 3, the study area and data source are introduced. Chapter 4 presents the whole methodology of this thesis. In Chapter 5, the analysis of ML models' application on snow mapping is given. Chapter 6 gives the conclusions, limitations, main findings of this study, and recommendations for future research areas.

Chapter 2

Research Context

2.1 Passive microwave remote sensing of snow cover

2.1.1 Theoretical basis

As shown in Figure 2.1, the PMW radiation transmission model describes the radiation and scattering process between the microwave through the rough surface, inhomogeneous dense medium (such as snow), and the atmosphere (Ulaby et al., 1981), which is the basis of PMW snow inversion. Because the snow layer is a non-uniform medium, the microwave has to go through multiple scattering and absorption processes. The ascending and descending radiation of the snow layer interface can be expressed by Eq. 2-1 and 2-2(Ulaby et al., 1981):

$$\mu_s \frac{dT^+}{dz} = -k_e T^+ + k_a T + F^+ \tag{2-1}$$

$$\mu_s \frac{dT^-}{dz} = -k_e T^- + k_a T + F^- \tag{2-2}$$

Where μ_s is the total upward radiation of the medium; z is the depth; T^+ and T^- are the radiation intensity above and below the snow layer respectively; k_e is the snow attenuation coefficient; T is the temperature profile of snow layer; k_a is the absorption coefficient of snow layer; F^+ and F^- are the upward and downward scattering term of the snow particles, respectively.

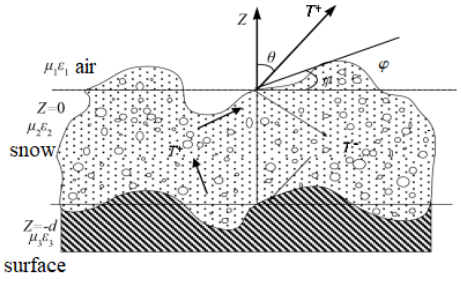

Figure 2. 1 Microwave emission from the surface and snow (Sun et al., 2015) where ε is the dielectric constant; θ is the incidence Angle; φ is the exit Angle.

Microwave radiation models of snow cover include scattering layer microwave emission model (England, 1975), the University of Helsinki's (HUT) snow emission model (Pulliainen et al., 1999), and the microwave emission model of layered snow snowpacks, MEMLS) (Wiesmann & Mätzler, 1999) and snow accumulation model based on dense medium radiative transfer (DMRT) theory (Tsang, 1992), and the Snow Microwave Radiative Transfer (SMRT) model (Picard et al., 2018).

The satellite microwave radiometer finally records the microwave radiation energy from the ground in the form of antenna temperature (TA) and then converting to brightness temperature (Tb) through calibration (Armstrong et al., 1993), which comes from four parts, which can be expressed by formula 2-3 (Figure 2.2):

$$Tb=Tb1+Tb2+Tb3+Tb4 \quad (2\text{-}3)$$

Where Tb1 is the energy emitted by the surface under the snow layer, Tb2 is the energy emitted by the snow layer, Tb3 is the sky radiation reflected by the snow-surface interface, and Tb4 is the sky radiation reflected by the snow-air interface. The energy of microwave radiation from snow mainly comes from the surface beneath the snow layer (Tb1) and inside the snow layer (Tb2) (Chang et al., 1987).

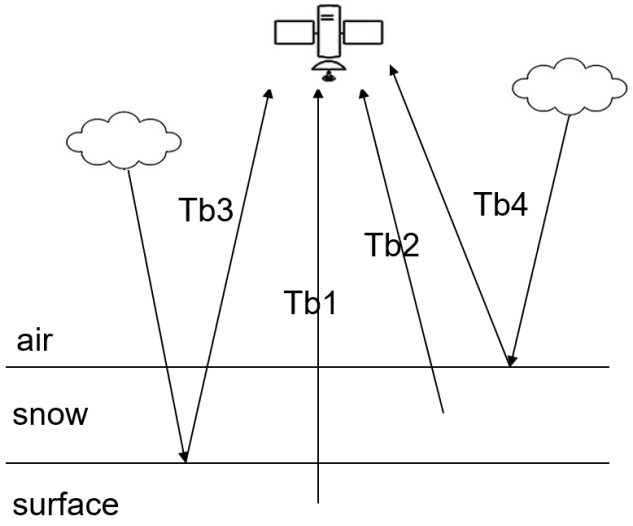

Figure 2. 2 Microwave radiation of the surface with snow cover

In the microwave radiation of snow, the bulk scattering of snow particles plays an important role, which can attenuate, and scatter part of the energy radiated from snow. The microwave radiation characteristics of snow will change with the changes in snow thickness, particle size (Hofer & Mätzler, 1980), snow density, snow temperature, moisture content (Hallikainen et al., 1987), snow structure, and underlying surface medium. The greater the depth of the dry snow cover, the more particles scattering microwave signals in the snow cover, and the more energy will be scattered in the process of penetrating the snow cover, resulting in less energy received by the satellite sensor and lower Tb (Chang et al., 1997). When the snow melts, due to the presence of liquid water in the snow layer, a large part of the microwave radiation energy of the snow is absorbed and cannot penetrate the snow layer. In the energy radiation of snow, the scattering effect is dominant, among which dry snow is a strong scatterer, and its scattering effect will be enhanced with the increase of microwave frequency (Ulaby et al., 1981).

2.1.2 PMW remote sensing snow data

Tb value provided by Satellite PMW sensors are used for snow detection. The widely used sensors include SMMR (Scanning Multichannel Microwave Radiometer) on Nimbus-7, SSM/I (Special Sensor Microwave Imager) and SSMIS (Special Sensor Microwave Imager Sounder) on DMSP (Defense Meteorological Satellites Program); AMSR-E (Advanced Microwave Scanning Radiometer-EOS) sensor on the Aqua satellite; AMSR2 (Advanced Microwave Scanning Radiometer 2) sensor on the GCOM-W1(Global Change Observation Mission-Water) satellite, and MWRI (Microwave Radiation Imager) on the FY-3 series satellite Sensors (Table 2.1).

Table 2. 1 Parameters summary of PMW sensors

Sensor	Platform	Time	Frequency/GHz	Polarization	Instantaneous field of view(km)
SMMR	Nimbus-7	1978.10-1987.08	6.6	H, V	136×89
			10.7	H, V	87×57
			18.0	H, V	54×35
			21.0	H, V	47×30
			37.0	H, V	47×30
SSM/I	DMSP	1987.07-2009.11	19.35	H, V	70×45
			22.24	V	60×40
			37.0	H, V	38×30
			85.5	H, V	16×14
SSMIS	DMSP	2006.12-	19.35	H, V	70×45
			22.24	V	60×40
			37.0	H, V	38×30
			91.66	H, V	38×30
AMSR-E	Aqua	2002.06-2011.10	6.93	H, V	75×43
			10.65	H, V	51×39
			18.7	H, V	27×16
			23.8	H, V	32×18
			36.5	H, V	14×8
			89.0	H, V	6×3
AMSR2	GCOM-W1	2012.05-	6.93	H, V	62×35
			7.3	H, V	62×35
			10.65	H, V	42×24
			18.7	H, V	22×14
			23.8	H, V	26×15
			36.5	H, V	12×75
			89.0	H, V	5×3
MWRI	FY-3B/3C	2010.11-	10.65	H, V	51×85
			18.7	H, V	50×30
			23.8	H, V	27×45
			36.5	H, V	18×30
			89.0	H, V	9×15

Since the launch of PMW sensors on the Nimbus satellite in 1978 and the DMSP series satellites in 1987, research on snow based on PMW remote sensing has rapidly advanced. Compared with SSM/I and SSMIS, the AMSR-E and AMSR2 sensors on the Aqua satellite and GCOM-W1 offer higher spatial resolution and more frequency bands, ranging from 6.9 to 89 GHz. The upcoming AMSR3, scheduled to launch in 2024, will have even more frequency bands, enhancing snow monitoring capabilities. The data from the five existing PMW sensors (SMMR, SSM/I, SSMIS, AMSR-E, and AMSR2) are available through the National Snow and Ice Data Center (NSIDC). To ensure maximum data consistency, all the data from these four sensors were sampled, and an Equal-Area Scalable Earth grid of 25 km × 25 km was used (EASE-Grid) for storage in the NSIDC (Armstrong & Brodzik, 1995). This allows the direct download of 25 km × 25 km data from NSIDC. The Equal-Area Polar Azimuth projection is used in the Arctic and Antarctic regions, while the Equal-Area Cylindrical projection is used for a global perspective.

2.2 Optical remote sensing of snow cover

2.2.1 Theoretical basis

Optical remote sensing of snow is mainly based on the difference in spectral characteristics of snow in visible light, near-infrared, short-wave infrared, and thermal infrared bands. Figure 2.3 shows a comparison of the spectral features of snow and other Earth features based on the Advanced Spaceborne Thermal Emission Reflection Radiometer (ASTER) spectral library, the ASTER spectral Library (Baldridge et al. 2009). The low reflection (high absorption) coefficient of snow at 1.5μm and 2.0μm is the important characterization to separate snow with other earth features. Because snow has strong reflection properties in the visible part and strong absorption properties in the short-wave infrared, the NDSI effectively distinguishes snow from many other surfaces. NDSI is defined as follows:

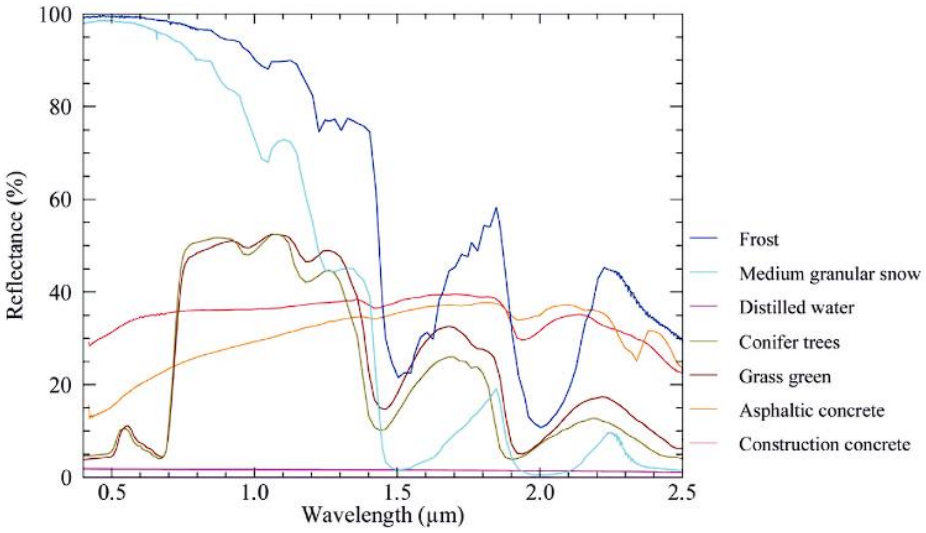

Figure 2. 3 Comparison of spectral signatures of snow and other earth features based on ASTER spectral library data (Baldridge et al. 2009)

$$NDSI = \frac{(b_4 - b_6)}{(b_4 + b_6)} \tag{2-4}$$

Where, b_4 and b_6 represent the reflectance values of MODIS band 4 (Visible Green) and band 6 (Shortwave Infrared Red, SWIR), respectively. In the process of utilizing NDSI for identifying snow pixels, the key factor to consider is establishing the detection threshold. The NDSI threshold of 0.4 serves as a commonly adopted global standard for distinguishing snow from non-snow in a binary manner (Zhang et al., 2019). The standard threshold of 0.4 needs to be adjusted on a local scale. For instance, the reflectance properties can vary on steep slopes or shaded areas, and the presence of a forested area can influence the way snow reflectance interacts with trees. However, since the study area is in the whole Arctic, 0.4 is still chosen as the threshold for snow identification.

2.2.2 Optical remote sensing snow

Optical remote sensing is a valuable tool for monitoring snow cover using visible and near-infrared bands. Various optical remote sensing products and sensors are employed for snow monitoring, including MODIS snow cover product, Landsat snow cover product, and

Sentinel-2, etc. MODIS offers lower spatial resolution (250-500 meters) compared to Sentinel (10-20 meters) and Landsat (30 meters). This makes MODIS more suitable for studies in larger scale. Also, MODIS has a higher temporal resolution, providing daily data, while Sentinel-2 and Landsat offer data less frequently (e.g., every 5 to 16 days). So, MODIS data was selected in this research. MODIS offers several snow products, each with specific purposes., such as product MOD10A1/MYD10A1 provides information on fractional snow cover (Collection 5) and NDSI values (Collection 6). Also, since the cloud effects on the snow detection by optical remote sensing, the cloud gap filled snow product are developed for the snow mapping, such as MOD10A1F product.

2.3 Machine learning applications - general principles

The selection of ML classification methods involves considering various aspects such as sample size, data complexity, the balance between interpretation and accuracy, the trade-off between speed and accuracy, and outlier processing. Therefore, data curation is a crucial step to ensure the quality and reliability of the dataset, directly impacting the performance and interpretability of chosen ML models. In this study, the dataset is large, and potential outliers may exist. While the Maximum Likelihood Method (MLC) offers faster convergence suitable for large-scale and high-dimensional data, it often assumes specific data distributions, such as normal distributions, which may not hold for real-world data. LR is a suitable choice for binary classification problems, but if the relationship is highly non-linear or involves intricate interactions between features, more complex models like SVM and RF could be explored. RF and SVM demonstrate good accuracy on non-linear data, although SVM may run slowly on large datasets. Both models are highly robust and suitable for handling outliers. Therefore, this study applied three ML methods—LR, RF, and SVM—with the same input for snow cover estimation.

2.3.1 Logistic Regression approach to ML

LR is a robust statistical method primarily employed in binary classification tasks, where the outcome variable involves two distinct classes (Hosmer et al., 2013). LR utilizes a

logarithmic probability function, transforming the linear regression equation via the Sigmoid function, which effectively maps any real number to a bounded range between 0 and 1. This characteristic makes LR well-suited for modeling probabilities. As a member of generalized linear models, LR employs the logistic function as its core, and parameters are estimated through the maximum likelihood method (Musa, 2013). The significance of each parameter is subsequently evaluated using rigorous statistical tests. In practical applications, LR model predictions are derived by setting a threshold, commonly at 0.5, where predicted labels are assigned based on whether the calculated probability exceeds this threshold, as shown below:

$$if\ probabilities\ of\ (y = 1) \geq 0.5, instance\ class\ (y = 1)$$
$$if\ probabilities\ of\ (y = 1) < 0.5, instance\ class\ (y = 0) \quad (2\text{-}5)$$

2.3.2 Random Forest approach to ML

The theory of RF shows in Figure 2.4. RF serves as a prominent ensemble learning technique extensively applied in the domains of classification and regression. The methodology entails the creation of multiple decision trees during the training phase, whereby each tree is constructed through an iterative process. Notably, the dataset denoted as T, encompassing N samples, undergoes bootstrapping, a resampling technique wherein N samples are randomly drawn with replacement. Subsequently, each decision tree is trained on its respective bootstrapped subset, employing a randomized selection of M attributes when nodes necessitate division, adhering to the condition m << M. The choice of the splitting attribute for a node is dictated by a specific strategy, such as information gain. This recursive partitioning continues until the nodes can no longer be split. The ensemble nature of RF is underscored by the independent generation of multiple decision trees through the bootstrapping process. Aggregating the predictions of these individual trees, the RF model derives its final prediction by discerning the category with the highest frequency of votes among the decision trees (Pavlov, 2000).

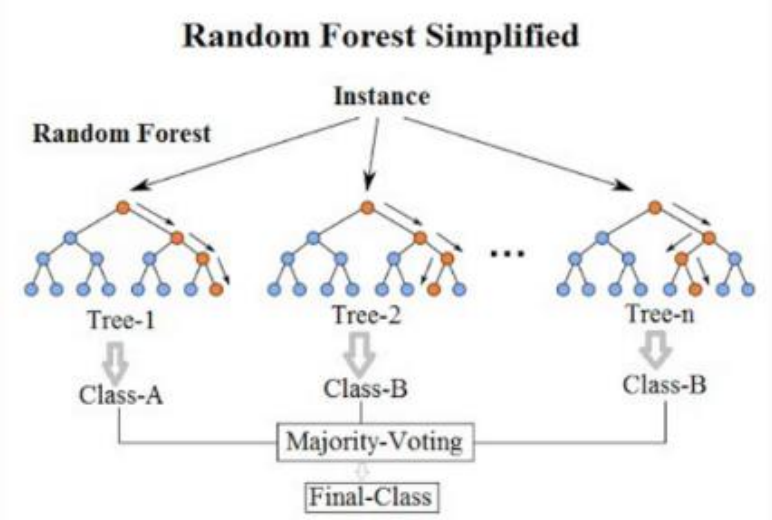

Figure 2. 4 Theory of RF Classifier (Source: https://gaussian37.github.io/ml-concept-RandomForest/)

2.3.3 Support Vector Machine approach to ML

The fundamental principle underlying SVM learning is the identification of distinct hyperplanes that effectively partition the training dataset while simultaneously maximizing the geometric margin, a concept elucidated by Joachims in 1999. A hyperplane can be conceptualized as a multidimensional surface that acts as a decision boundary, demarcating different classes in the feature space. The goal is to find the hyperplane that maximizes the margin between classes, thereby enhancing the model's generalization capability.

To address non-linear classification challenges inherent in the input space, SVMs leverage the concept of nonlinear transformations, allowing the conversion of non-linear problems into linear tasks within a higher-dimensional feature space. This process facilitates the establishment of linear SVM models, offering a powerful approach to complex classification scenarios. In the realm of high-dimensional remote sensing data analysis, the utilization of kernel functions becomes imperative (see Figure 2.5). Kernel functions play a pivotal role in SVMs by projecting the input dataset into a higher-dimensional feature space, where the training samples become linearly separable. These kernel functions, including Sigmoid, Radial Basis Function (RBF), Polynomial, and Linear, enable SVMs to address

intricate patterns in the data. Notably, in remote sensing applications, the RBF and Polynomial kernels are commonly employed owing to their efficacy in capturing complex relationships within spatial and spectral data (Cherkassky & Ma, 2004).

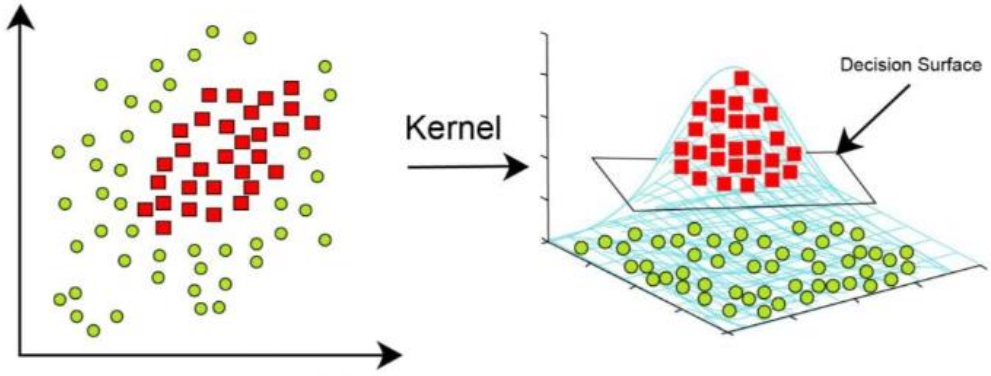

Figure 2. 5 Theory of Support Vector Machine Classifier (Source: https://www.slidestalk.com/s/support_vector_machines_1rduvu)

2.3.4 Application of ML to remote sensing of snow

ML is increasingly being applied to snow mapping and snow parameter retrieval (snow depth (SD), snow water equivalent (SWE)). LR is commonly used for modeling a binary dependent variable. By using a simpler calculation, LR avoids the complications of multicollinearity that can arise with numerous variables (Whyte et al., 2018). RF is not sensitive to the misclassification of pixels although the presence of clouds and forests can affect snow cover detection (Luo et al., 2022). SVM is another commonly used classification algorithm. It is a powerful method in nonparametric classification and does not assume a known statistical distribution of the data to be classified (Chutia et al., 2016). Compared with RF, SVM has more classification applications in land use, agriculture, and cities and is mainly targeted at multispectral and hyperspectral remote sensing images (Sheykhmousa et al., 2020). LR seldom used in snow research, and in snow research, RF and SVM model usually used for estimate SD and SWE. For example, SD or SWE are estimated using SVM or RF based on microwave and optical data (Kwon et al., 2019; Xiao et al., 2018; Liang et al., 2015). In

addition, RF-based regression performs better than SVM in snow depth retrieval (Wei et al., 2022).

2.4 Considerations in combining PMW and optical data in ML for snow cover mapping

Therefore, other high-resolution remote sensing image data or products, such as MODIS data, have been fused with PMW remote sensing data for processing so that the data after fusion can better express the heterogeneity within the coarse resolution pixels of PMW remote sensing data and improve the utilization of multi-source data, complementary advantages make up for the defects of respective sensor data. There has been research into snow mapping using PMW and optical imagery. For example, a blended visible (Moderate Resolution Imaging Spectroradiometer, MODIS), PMW (Advanced Microwave Scanning Radiometer for the Earth Observing System, AMSR-E), and Quick Scatterometer (QuikSCAT or QSCAT) global snow product was proposed by Foster (et al., 2011). The PMW data were used to fill the areas where MODIS data was under cloud or darkness, and AMSR-E snow product and QSCAT can detect the melting areas. Bergeron (et al., 2014) created a combined snow product by merging data from AMSR-E and MODIS. This study aimed to enhance the accuracy of streamflow predictions resulting from snowmelt in the spring season.

The previous studies (e.g. Foster et al., 2011) aimed to develop a more accurate snow cover product by blending the multi-source data. In addition, the snow detection algorithms of PMW and optical data are generally used in a large scale. But the different elevations and surfaces beneath the snow also affect the detection accuracy. Those influences will reflect on the change of some parameters, e.g., Tb, and ML can learn the relationship between input and output from the amount of data. So, ML methods are expected to achieve better classification accuracy to a large extent with complex terrain. With the diversification and quantification of satellite remote sensing data, a major advantage of ML is that it can effectively cope with high-dimensional and massive data for pattern recognition and classification, which can solve the limitation of traditional remote sensing on accuracy and efficiency.

There are few studies on SCA detection using ML based on PMW data. The reason is that ML performs better in parameter retrieval of regression models, binary snow detection is relatively simple compared with SWE and SD retrieval, and binary snow cannot provide deeper snow information except snow distribution. However, accurate snow cover mapping is the basis for further study of snow cover parameters. Snow mapping has always been an important work in studying the cryosphere. Since SCA is more straightforward to identify in optical than microwave, microwave-derived snow cover is commonly used to fill MODIS clouds and dark regions (Foster et al., 2011). Therefore, the combination of PMW and MODIS can improve the accuracy of snow mapping. Although various snow cover algorithms can get satisfactory classification results, using ML for PMW SCA detection can explore the ability of PMW in snow cover detection and promote the development of ML in remote sensing classification.

Building on the foundation established by Xiao et al. (2021), who conducted research on estimating FSC from PMW data using ML techniques, this research is inspired by their achievements. While Xiao et al.'s (2021) work demonstrated the efficacy of utilizing enhanced Tb and MODIS snow product, this research aims to enhance this exploration by incorporating different PMW datasets alongside MODIS snow product, thereby improving the accuracy and robustness of snow mapping. By applying various ML approaches tailored to the unique characteristics of the datasets at my disposal, this research seeks to contribute novel insights and methodologies to the field of snow cover analysis.

Thus, this study aims to develop a feasible ML method utilizing the PMW Tb data and MODIS binary snow product data to estimate daily snow cover area at a 25 km resolution.

Chapter 3

Study Area and date source

3.1 Study Area

To consider only those areas covered by snow on the land, the study area obtained over the Arctic is shown in Figure 3.1. Greenland and Iceland were excluded because the snow area of those regions is usually snow on ice and glaciers, but this study focus on snow on land. Also, areas with a high-water fraction affect the microwave response, which results in uncertainties in snow detection. Water fractions from the Global Lake and Wetland Database (GLWD) level 1 product (Lehner & Doll, 2004) were also considered in this study. Water fraction data are 12.5 km EASE-Grid 2 projection data created using the average of 1 km data in a 12.5 km EASE grid cell. 10% WF was selected for the water mask because the majority water body can be masked.

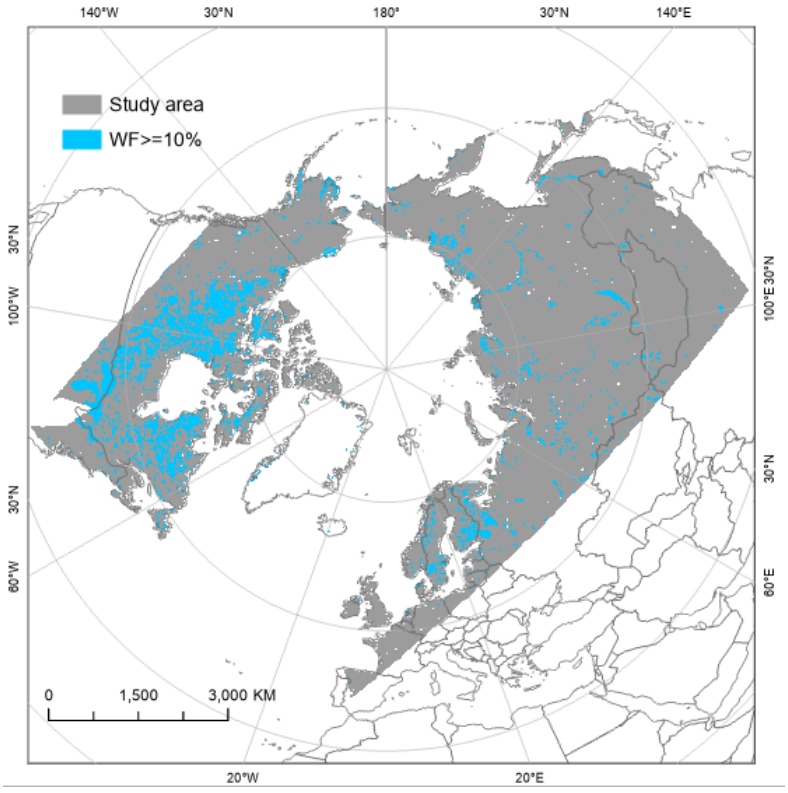

Figure 3. 1 Study area (EASE grid 2.0 North)

3.2 Data Source

3.2.1 PMW Tb data sources

The Tb data used in this research is the AMSR-E/2 Unified L3 Daily 25 km Brightness Temperatures, obtained from the National Snow and Ice Data Center (https://nsidc.org/data/au_si25/versions/1). This dataset includes six frequencies of 6, 10, 18, 23, 36, and 89 GHz, and each frequency has two horizontal and vertical polarization modes. The data has a spatial resolution of 25 km, projected NSIDC Sea Ice Polar Stereographic North and the data format is HDF-EOS5. The GCOM-W1 satellite has two transit times a day, the transit time of the orbit is 13:30 (±15 min), and the orbit is 01:30 (±15 min). Liquid water in the snow will absorb part of the microwave radiation energy (Sun et al., 2006). Therefore, the transit time of the ascending orbit is affected potentially by snowmelt. This study selects the descend data for the snow monitoring in the Northern Hemisphere.

3.2.2 MODIS snow product

MODIS Collection 6 product uses NDSI value instead of fractional-snow cover (FSC) to provide the snow information. This product remains globally and can also be applied to an algorithm to derive FSC from NDSI in a particular study area (Hall et al., 2019). Cloud cover is the significant factor affecting snow mapping accuracy using VNIR. The cloud issue can be mitigated by cloud-gap filling (CGF). Many methods have been developed to eliminate the snow cover in the MODIS snow cover suite.

This study selected MODIS snow products as reference data because of their wide application and high accuracy. The data set (MOD10A1F) provides 500 m resolution daily cloud-free global snow cover derived from the MODIS/Terra Snow Cover Daily L3 Global 500m SIN Grid data set (MOD10A1) (https://nsidc.org/data/mod10a1f/versions/61). This CGF daily map is generated by retaining a previous day's non-cloud observation when the current day has a cloud. A separate parameter is provided as cloud persistence count (CPC), which tracks the number of days in each cell since the last clear-sky observation. Another used band of this dataset is 'Basic_QA', which provides a general quality estimate for pixels processed

for snow. The advantage of this product is that a user can decide how far back in time they would like to use observation and use the CPC information to develop a unique CGF map appropriate for their application.

MOD44B Vegetation Continuous Filled (VCF) product is also used in this research to provide a global representation of forest cover at 250 m pixel resolution. Snow mapping with PMW Tb data in forest region is always a key challenge because the forest canopy can attenuate microwave radiation from the underlying snow and create additional emissions, thereby influencing the accuracy of snow detection. This study will consider the snow mapping accuracy on a different forest fraction (FF) level. According to the previous study about the impact of FF on PMW measurements, even a minimal forest fraction (FF) of 0.2 can cause notable alterations in the PMW measurement, with deviations of up to 10 K, and when FF surpasses 0.6, it can obscure nearly all the microwave signals associated with snow (Vander Jagt et al., 2013). Figure 3.2 is an example of FF which in 2018, three classes of FF were applied: high (FF>60%), medium (20%<FF<=60%) and low (FF<=20%).

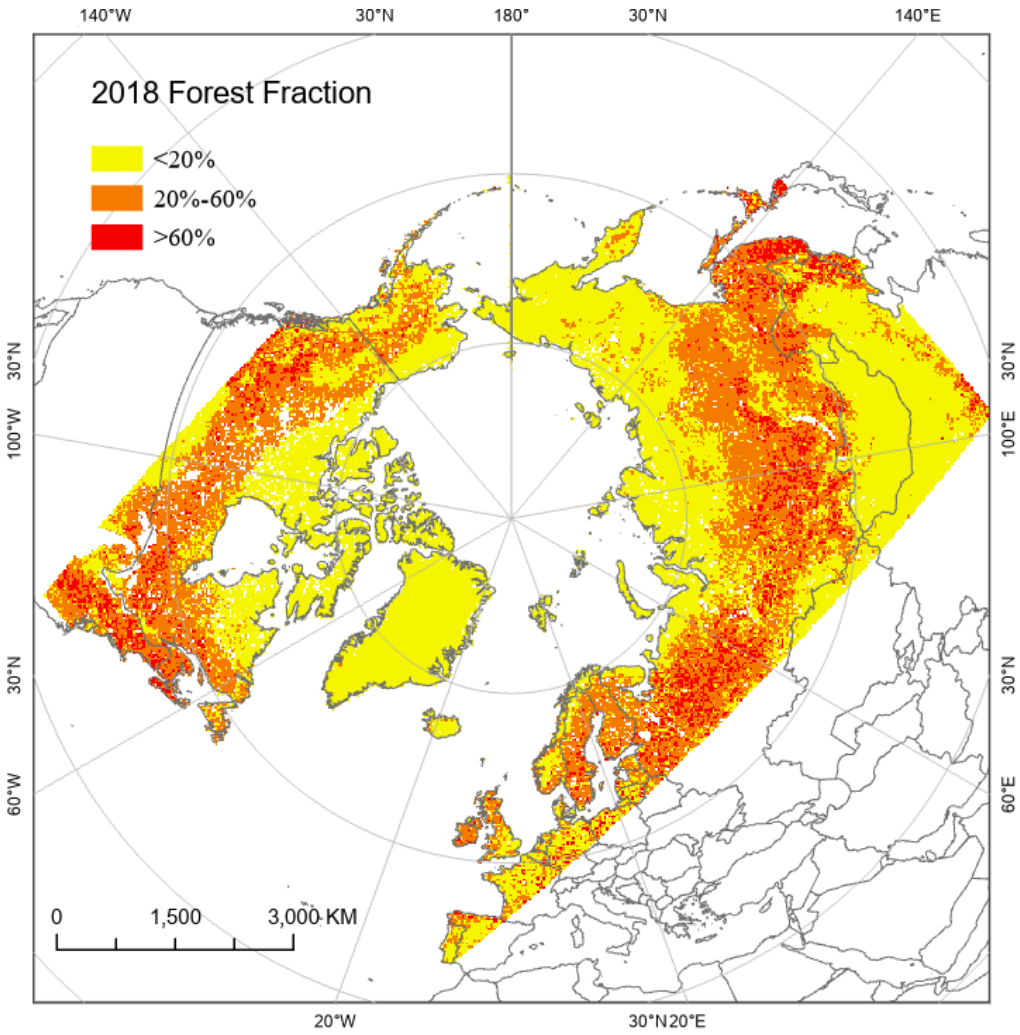

Figure 3. 2 The forest fraction map in 2018 (EASE grid 2.0 North)

3.2.3 Seasonal snow classification data source

The snow classification dataset serves as a vital reference source, offering valuable physical and climatological insights into snow. The physical characteristics of snow are closely related to its Tb values. When assessing snow mapping, seasonal snow classification is considered by developing retrieval models based on different snow classes obtained from seasonal snow classification data. The seasonal snow cover classification map was obtained from the NASA National Snow and Ice Data Center (NSIDC). This classification system, as proposed by Sturm et al. in 1995, and improved by Sturm & Liston, 2019, is founded on the

distinguishing features of various snow layers. The dataset is available at four spatial resolutions, approximately 300 meters, 1 kilometer, 5 kilometers, and 50 kilometers, with this study utilizing the 5-kilometer resolution data. The snow classes encompass tundra, taiga maritime, ephemeral, prairie, alpine, and ice (refer to Figure 3.3). For the purposes of this study, the focus is placed on the most prominent snow classes, including tundra, taiga, prairie, and alpine.

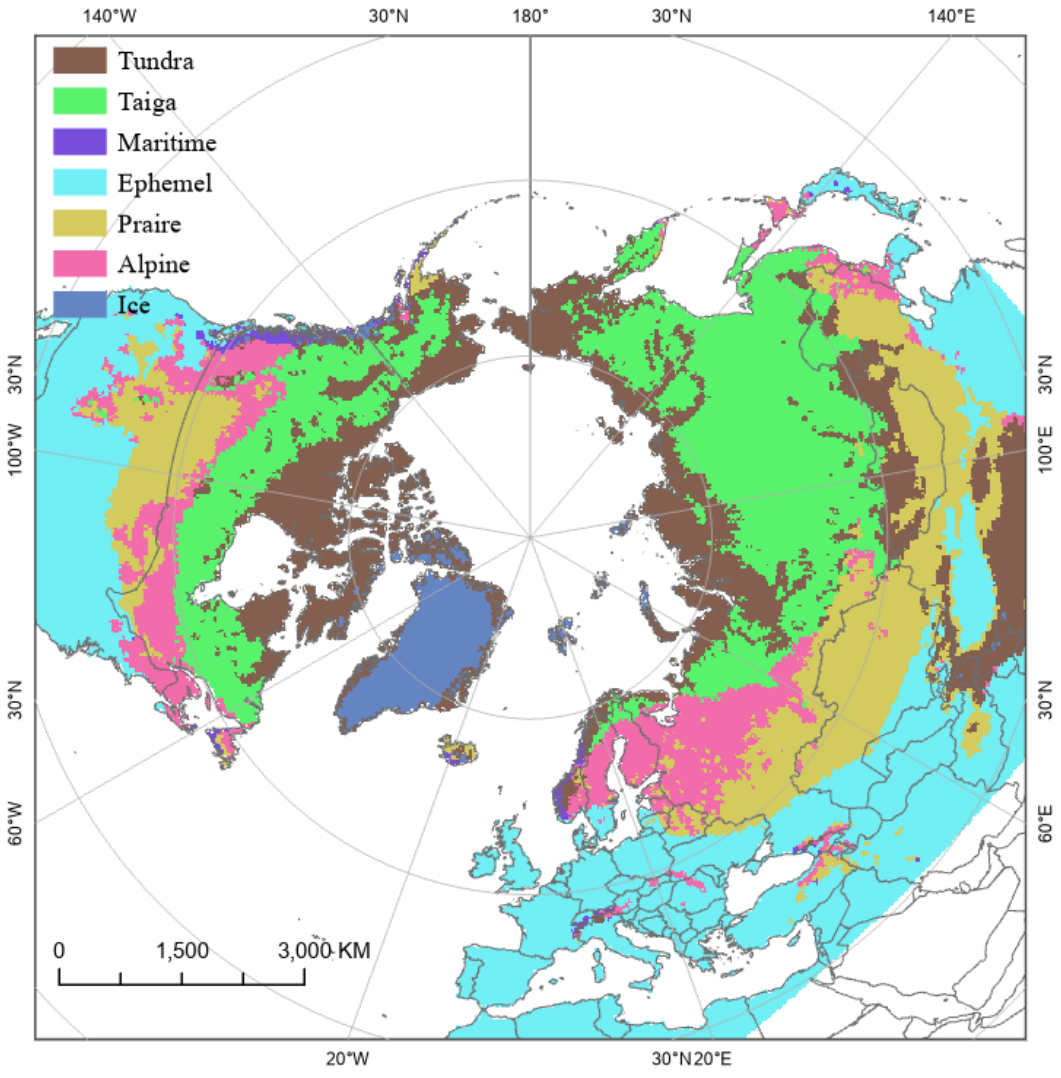

Figure 3. 3 Seasonal snow classification from Sturm et al. (1995) presented in an EASE grid 2.0 North projection.

3.2.4 Snow depth data source

The Canadian Meteorological Centre's daily snow depth analysis data, archived at NSIDC (https://nsidc.org/data/nsidc-0447/versions/1), was chosen as the comparative dataset for evaluating the SCA map estimated through ML. This dataset was created by assimilating real-time, in-situ daily snow depth observations using optimal interpolation with a first-guess field, as described by Brown & Brasnett in 2010. The initial estimates are derived from a fundamental model that computes snow accumulation and melting. This model integrates analyzed temperature data and six-hour precipitation forecasts sourced from the CMC Global Environmental Multiscale (GEM) forecast model, as detailed in Brown & Brasnett's work from 2011. The data is presented on a 24-kilometer polar stereographic grid, which aligns with the PMW data. The northern hemisphere coverage includes daily snow depth analysis, average snow depth, climatology, and estimates of snow water equivalent (SWE). It's important to note that sparse data coverage over Canada and Russia may introduce uncertainties, as the snow depth data in these areas is primarily generated from the background field. Additionally, specific snow depth measurements are conducted in exposed, uncovered locations. These areas typically receive and retain less snow, leading to more rapid snow cover diminishment compared to the surrounding terrain. However, these issues are more likely to result in a significant bias in snow depth rather than affecting the snow cover extent. The SCA map can be generated from CMC data by applying a defined snow depth threshold. A snow depth example is provided in Figure 3.4.

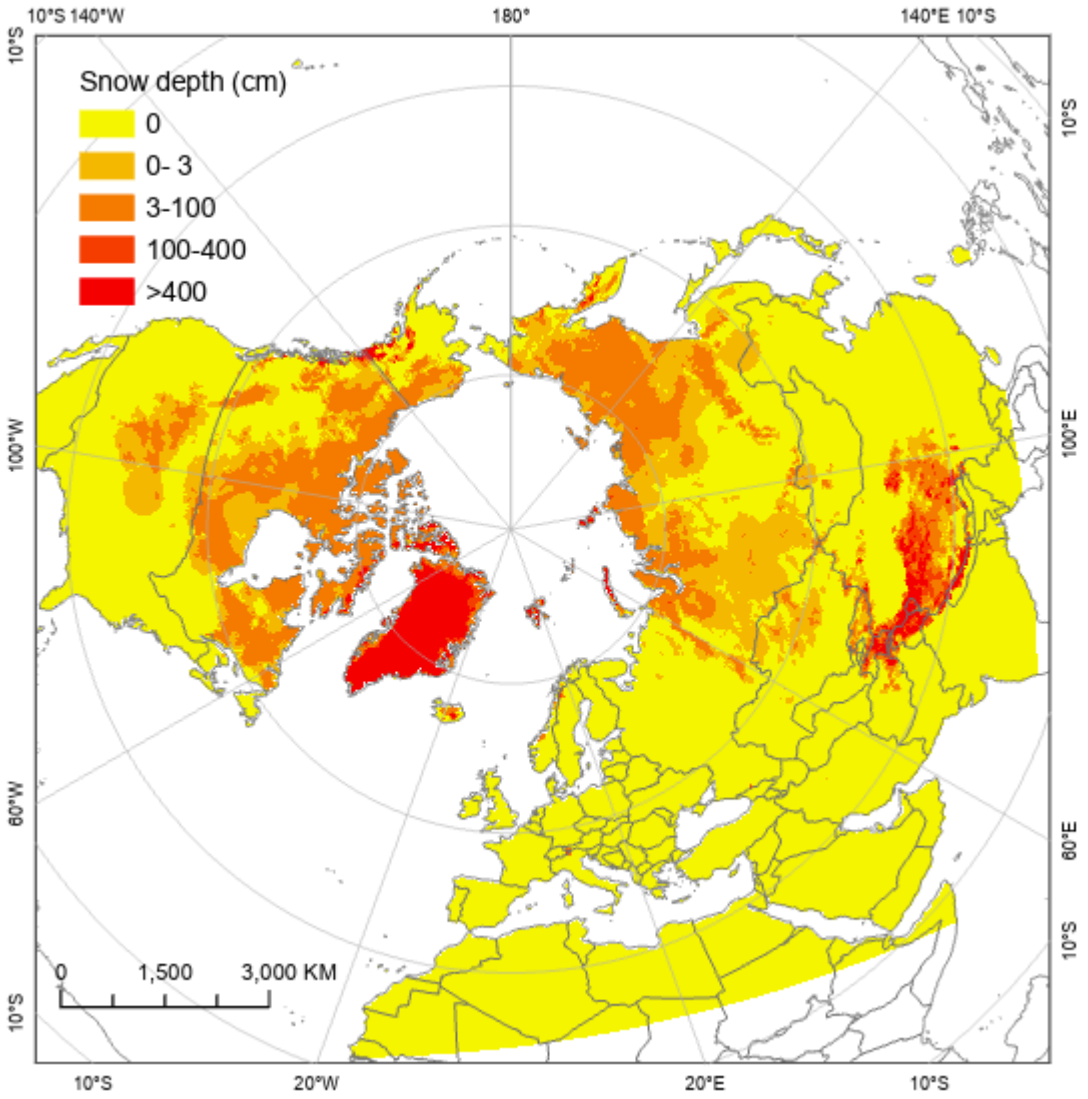

Figure 3. 4 The snow depth map from 2018 Oct.15 presented in an EASE grid 2.0 North projection.

Chapter 4

Methodology

4.1 Processing methods

Figure 4.1 is the workflow of this research. In this study, four different SCA datasets were generated using various data sources and methodologies. The SCA based on Tb data was derived using Grody and Basist's (1996) algorithm. The MODIS-SCA was obtained from the MOD10A1F snow product. The SCA obtained through ML was developed by utilizing Tb data and MODIS snow reference data as training variables. Additionally, the SCA based on CMC snow depth data was also included. Subsequently, an evaluation of ML's predictive capabilities for SCA was conducted by comparing PMW-SCA, MODIS-SCA, and ML-SCA. Furthermore, a performance assessment of the ML-SCA model was carried out by comparing it with CMC-SCA. This comprehensive analysis aimed to assess the effectiveness of ML in predicting SCA and further validate the model's performance.

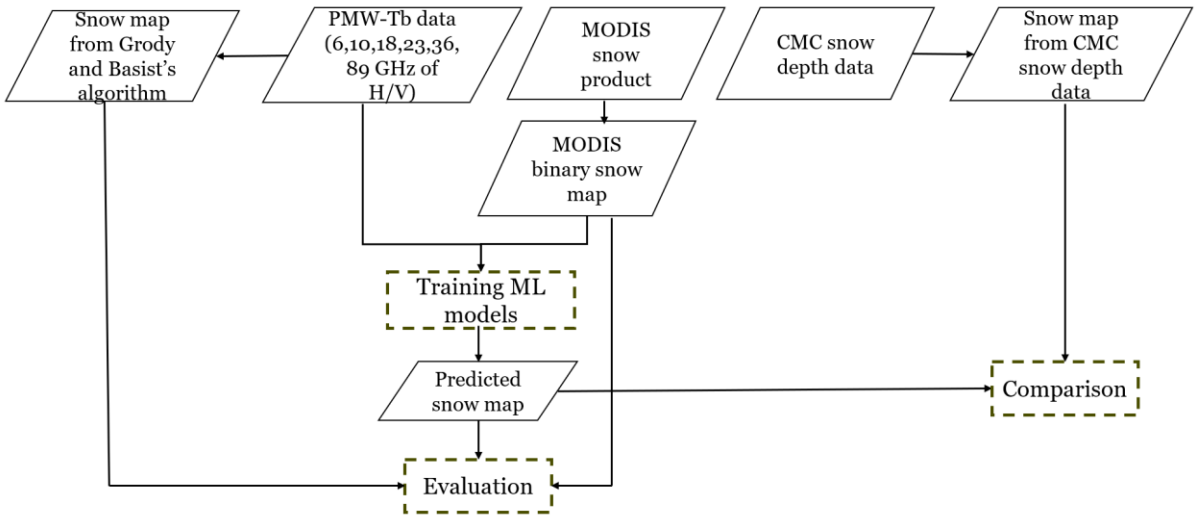

Figure 4. 1 workflow of the research

4.1.1 Preprocessing

All the datasets used were converted into the GeoTIFF format and resampled to 25 km using nearest neighborhood method. The Tb data projection was changed from Polar

Stereographic projection to the EASE grid since the Polar Stereographic projection is more suitable for sea ice but has more distortion further south. MODIS data is initially provided in tile format, so these tiles were merged to cover the same extent as the Tb data.

4.1.2 Snow cover identification

4.1.2.1 Snow identification by Grody and Basist's algorithm (1996)

Through the analysis of microwave Tb data and known surface characteristics, classification criteria were established, and a decision classification tree was developed to identify and remove snow-free pixels. In a study conducted by Zschenderlein et al. (2023) to evaluate different dry snow detection algorithms in the Northern Hemisphere, the results indicated that Grody and Basist's decision tree algorithm (1996) performed the best when compared to in-situ data. Therefore, this snow detection algorithm was chosen for use in this study. Grody and Basist's algorithm was originally proposed based on SSM/I measurements, which used antenna temperature (Ta) data. Since this study employs Tb data from AMSR-E/2, it was necessary to adapt the decision tree from Ta values to Tb values. To derive brightness temperature (Tb), a correction is applied by adjusting the temperatures from different frequency channels using respective offsets. Specifically, corrections of approximately 7K, 6K, 4K, and 3K are employed for the 18, 23, 36, and 89 GHz channels, respectively. Using this method, the extracted snow area was determined after filtering out non-scatterers, precipitation, cold desert areas, and frozen ground. Therefore, the revised snow cover decision tree of Grody and Basist's algorithm (1996), was applied to AMSR-E/2 PMW Tb data over land (as shown in Table 4.1). Figure 4.2 displays the extent of snow cover as of April 25, 2016, obtained using Grody and Basist's algorithm (1996).

Table 4. 1 The description of the revised decision tree algorithm by Grody and Basist (1996). The unit is Kelvin (K)

Scattering materials	**Identification conditions**
Scattering signature	1. Tb18V-Tb36V>3 or Tb23V-Tb89V>3
Precipitation	1. Tb23V>=265K or 260K<=Tb23V<=264K 2. Tb18V-Tb36V<=5K)
Cold deserts	1. Tb18V-Tb18H>=18K 2. Tb18V-Tb36V<=13K 3. Tb36V-Tb89V<=11K
Frozen ground	1. Tb18V-Tb18H>=8K 2. Tb18V-Tb36V<=5K 3. Tb23V-Tb89V<=9K

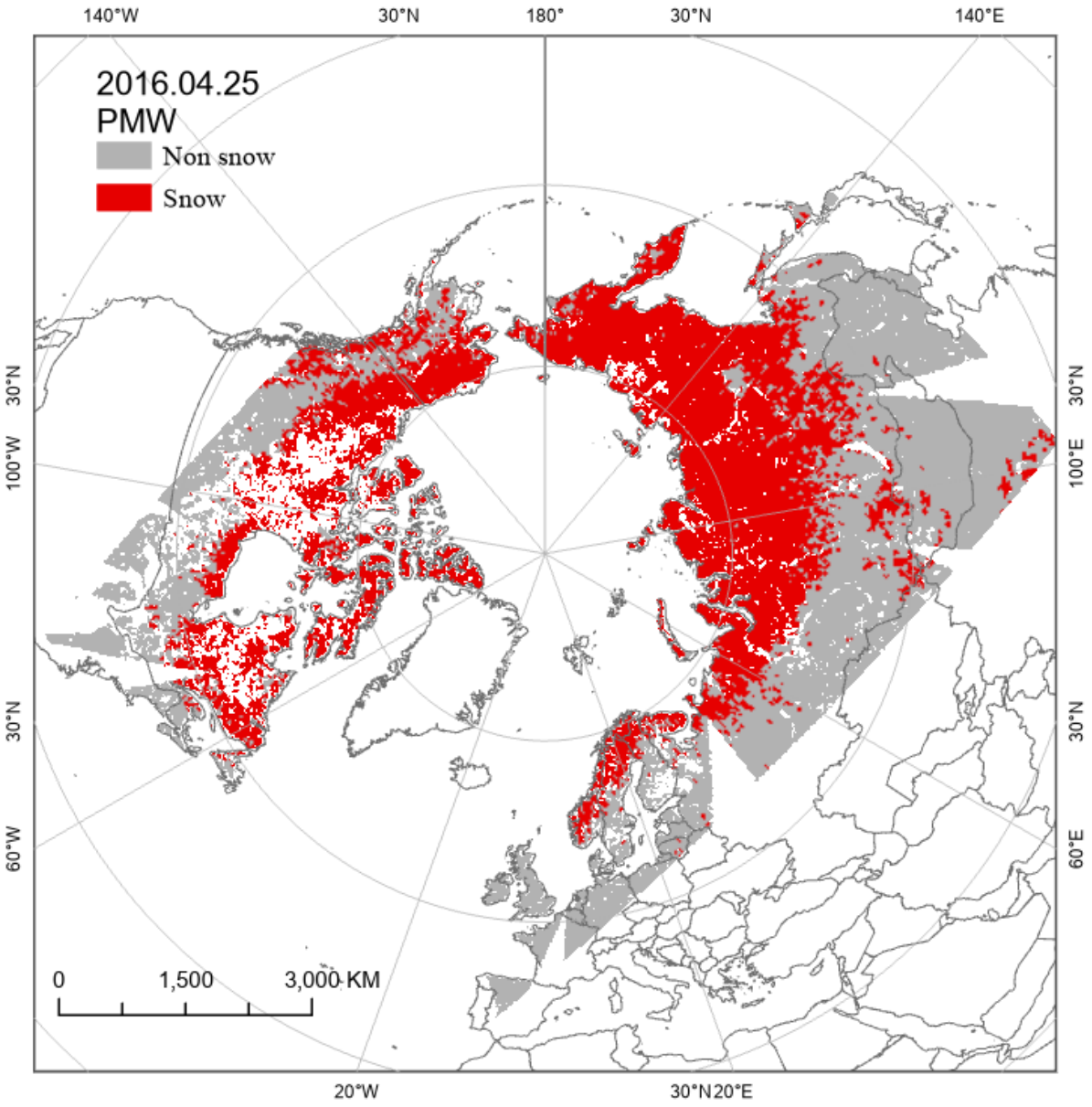

Figure 4. 2 An example of SCA generated by Grody and Basist's algorithm (1996) presented in an EASE grid 2.0 North projection.

4.1.2.2 Snow cover generation by MODIS

Xiao et al. (2021) employed the MOD10C1 snow product in their study, necessitating a preprocessing step to eliminate clouds from the dataset. In this research, the adoption of the CGF snow product was motivated by its enhanced effectiveness in generating precise snow maps. The deliberate selection of a more robust snow product aligns with the objective of enhancing the quality and reliability of the input data for subsequent ML analyses, thereby contributing to a more accurate representation of snow cover in the study area.

The parameters 'CFG NDSI Snow Cover,' 'Cloud Persistence,' and 'Basic_QA' were extracted to formulate the MODIS-SCA dataset. 'CFG NDSI Snow Cover' stores 8-bit unsigned integers, where values ranging from 0 to 1 denote fractional snow cover (ranging from no snow to completely snow-covered) (Figure 4.3a). A global reference of NDSI > 0.4 was chosen as the threshold for identifying snow pixels (Riggs et al., 2016). The 'Cloud Persistence' parameter signifies the number of consecutive days with cloud cover preceding the current day (Figure 4.3b). Snow pixels with higher values of CPC may lead to misclassifications. Typically, a nearly cloud-free map can be generated in five to seven days, contingent on the season and location (Hall & Riggs, 2020). In this paper, a threshold of seven persistence days was employed to map snow cover from MODIS. Consequently, pixels with more than seven persistence days were excluded from the dataset for ML analysis. While this threshold can result in an almost cloud-free map, there remains some uncertainty to be acknowledged. For instance, if cloud cover persists for fewer than two days, the gap-filling product may be deemed to have a high level of confidence and accuracy. However, if cloud cover persists for over five days, the confidence level is considered to be low. Figure 4.3c illustrates the final snow map for April 25, 2016, where NDSI > 0.4 and CPC ≤ 7.

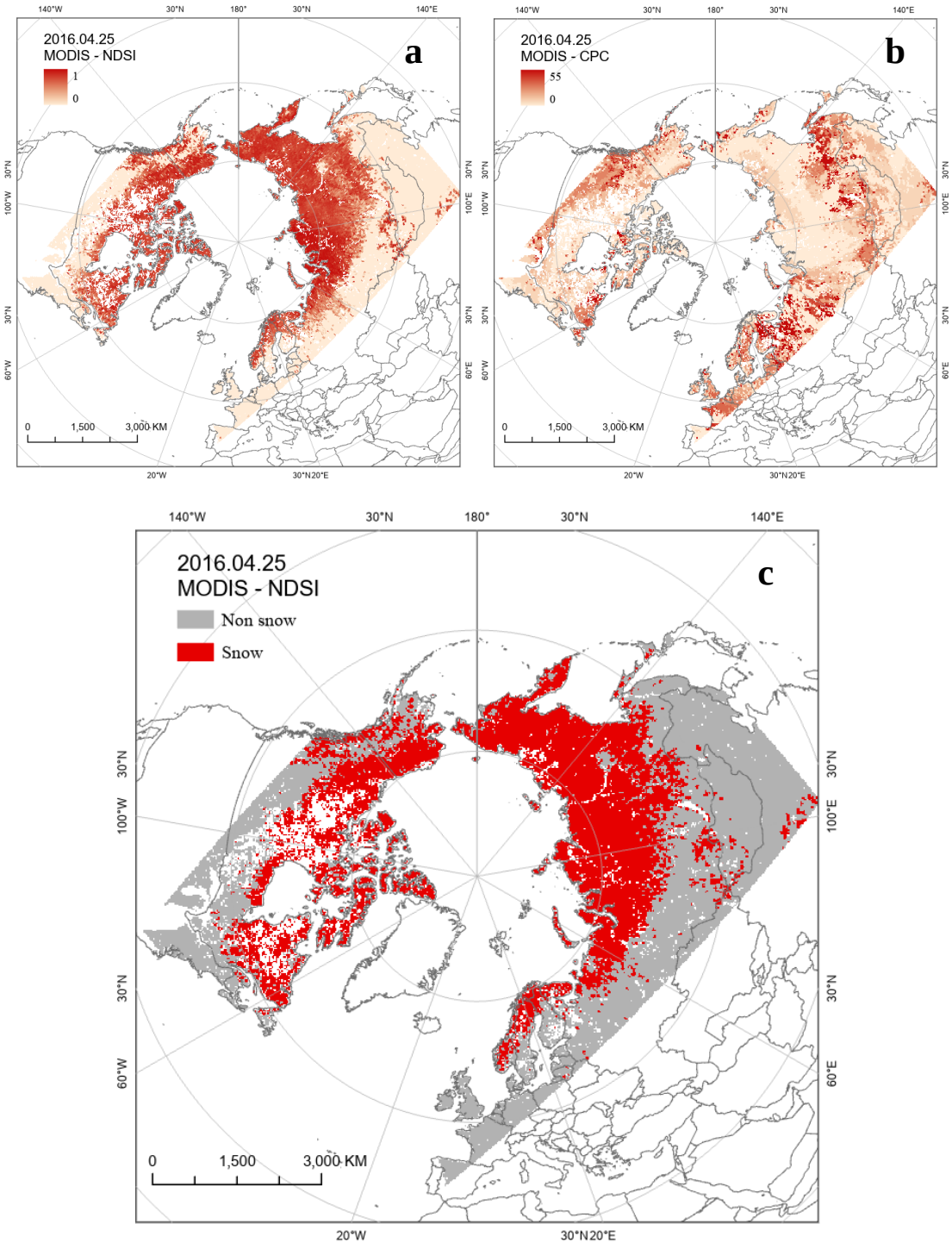

Figure 4. 3 MODIS snow product. a: NDSI, b: CPC, c: Binary snow map (NDIS>0.4 and CPC<=7) presented in an EASE grid 2.0 North projection.

4.1.3 ML application for snow detection

Since the original decision tree snow detection algorithm by Grody and Basist (1996) was proposed based on the SSM/I dataset, the frequencies of the sensor are not consistent with those of AMSR-E/2. For instance, the 85GHz of SSM/I is 89GHz in AMSR-E/2. Therefore, using the Grody and Basist's algorithm (1996) for snow detection may introduce uncertainties. In contrast, optical images can capture surface features more realistically and directly than PMW. MODIS snow products generally exhibit an estimated accuracy of over 90% worldwide (Hall & Riggs, 2007). For example, in a research study conducted by Klein and Barnett (2003), the MOD10A1 MODIS snow products demonstrated an accuracy rate of 94.2% when compared to data from 15 SNOpack TELemetry (SNOTEL) sites. Hence, there is an expectation that ML-based snow monitoring would outperform Grody and Basist's algorithm (1996). In the ML approach, Tb channels and the MODIS SCA were used as input data. The input data consisted of Tb values at six frequencies (6, 10, 18, 23, 36, 89 GHz) with both horizontal and vertical polarizations, along with the MODIS binary snow data. Each pair of datasets comprises 13 parameters, and the binary snow value, as shown below:

Table 4. 2 The input variables and output variable for ML model

Input variables	Tb_06H, Tb_06V, Tb_10H, Tb_10V, Tb_18H, Tb_18V, Tb_23H, Tb_23V, Tb_36H, Tb_36V, Tb_89H, Tb_89V (in Kelvin)
Output variable	Snow (snow: 1 or non-snow: 0)

By establishing the correlation between each pair of Tb values and their corresponding output (MODIS binary snow data), the model gains the ability to predict new datasets post-training. This predictive capacity hinges on the utilization of solely Tb data as input, producing binary snow values as output. In contrast to Xiao et al.'s (2021) research, which employed Tb differences as input variables, our study incorporates all individual frequency Tb values. This selection is based on the autonomous learning capabilities inherent in ML algorithms, enabling

them to identify complex relationships among variables without explicit reliance on the physical information of input features. Two tasks were undertaken based on the training set: one utilized all individual frequencies as input variables, and the other incorporated frequency differences into the original variables. The results indicated negligible differences in the accuracy of these two models. The inclusion of all individual frequency Tb values in the model aims to maximize the information available for training, considering the possibility that the variable 18V-36V might become redundant if both 18V and 36V are already integrated as independent variables. This approach reflects a strategic consideration of optimizing the available information for robust model training. This approach is designed to exploit ML algorithms' inherent learning capabilities, facilitating the discernment of intricate patterns within the data and ultimately enhancing the model's proficiency in accurately mapping snow cover based on the provided input features. In Xiao et al.'s (2021) study, RF demonstrated superior performance among the ML methods investigated. So, in the current research, a deliberate decision has been made to include RF as one of the selected ML methods, given its proven efficacy in estimating fractional snow cover from PMW data. Additionally, this study uses LR and SVM, which were not explored in Xiao et al.'s (2021) research. The purpose of this expanded ML methodology is to assess the comparative effectiveness of RF alongside LR and SVM in the specific context of snow mapping using diverse input features. This diversification aims to contribute to a comprehensive understanding of the strengths and limitations of different ML approaches for the given research objectives.

The dataset utilized in the ML approach spans the timeframes of Oct, Dec, Feb, and April, covering the years 2012 to 2022, with the dataset division detailed in Table 4.3. The rationale behind selecting these specific months is rooted in the intention to comprehensively encapsulate the entire snow evolution cycle. This strategic choice aligns with the typical progression of snow-related phenomena: frozen ground emerging in low latitudes around Sep, the onset of snow in Oct, the revelation of depth hoar in Dec, a stable period of snow accumulation in Feb, and the initiation of snowmelt by Apr. By incorporating these specific months, the dataset effectively spans the diverse stages of the snow evolution cycle. While

recognizing the similarities in features among adjacent months from Sep to Apr, the deliberate selection of representative months serves a crucial purpose. It ensures that the ML model receives enough information to discern the necessary patterns, facilitating effective model training and verification. In the subsequent phase, the model trained on data from Oct, Dec, Feb, and Apr will be applied to validate data from other months. This step serves as a robust evaluation, gauging the model's performance and adaptability across various timeframes. This meticulous approach not only enhances the model's predictive capabilities but also validates its reliability in accurately capturing snow cover dynamics throughout the entire year. Daily AMSR-E/2 PMW Tb data (nighttime orbit only), and MOD10A1F SCA data for each of these months was used in the training, testing and validation steps.

Table 4. 3 Divide the dataset into training set, testing set and validation set

Training set	2013,2014,2015,2016,2017, 2020, 2021
Validation set	2012, 2022
Testing set	2018, 2019

4.1.3.1 Hyper parameter tunning and model comparison

Hyperparameters are parameters that users can set before training an ML model. All the three models were hyperparameter tunned. GridSearchCV method was used to filter the parameters that performed best for each model. The GridSearchCV approach involves systematically tuning parameters within a specified range. It adjusts these parameters in increments and proceeds to train the ML model with the adjusted settings. The ultimate goal is to identify the parameter configuration that yields the highest accuracy when evaluated on the validation dataset. This process encompasses both training and testing models with various parameter combinations (Liashchynskyi, & Liashchynskyi, 2019). GridSearchCV ensures the discovery of the parameter configuration that delivers the highest accuracy within the predefined parameter range. However, this advantage comes with a drawback. It necessitates the examination of all feasible parameter combinations, which becomes quite time-intensive

when dealing with extensive datasets and multiple parameters. Therefore, a smaller dataset comprising 2000 samples from validation set was chosen for the reference, given the computational demands.

The parameters need to be tuned for each model given in Table 4.4. For LR, the primary hyperparameter to fine-tune is the regularization strength, denoted by the parameter 'C.' The 'C' parameter influences the regularization term, balancing the desire to closely fit the training data with the goal of avoiding overfitting. A smaller 'C' value increases the regularization strength, leading to a simpler model, while a larger 'C' allows the model to capture more intricate patterns in the training data. Tuning the 'C' parameter is crucial for achieving the right balance between bias and variance in the LR model, ensuring robust generalization to unseen data. Additionally, the choice of optimization solver, such as ‘newton_cg’,'lbfgs' or 'liblinear,' can impact the model's convergence and efficiency.

For RF, the parameters that require adjustment are the number of decision trees (n_estimators) in the forest and the maximum depth of the tree. Generally, a small number of estimators may lead to underfitting, and the computational load increases as the n_estimators increase. Therefore, a moderate value is typically selected. The decision tree model first splits all the datasets and then continues the split process on the sub-datasets. The max_depth parameter limits the number of cycles and adding more splits to the trees can result in better classification, as long as the model does not overfit.

Within the SVM classification model, there are two essential hyperparameters: the penalty coefficient 'C' and the coefficient γ associated with the Radial Basis Function (RBF) kernel function. The penalty coefficient 'C' serves as a relaxation variable. Larger values of 'C' increase the loss function, resulting in more complex models for support vectors and hyperplanes, making them prone to overfitting. Conversely, smaller values of 'C' designate fewer samples as support vectors, resulting in a simpler final support vector and hyperplane model. As for the coefficient γ, it governs the impact of an individual sample on the overall classification hyperplane. Higher values of γ increase the influence of each sample. The default value in scikit-learn is

$$\frac{1}{number\ of\ sample\ features} \tag{4-1}$$

Table 4. 4 The parameters need to be tuned for each model.

Model	Parameter
LR	Penalty:defines penalization norms Solver: Provides options to choose solver algorithm for optimization.
RF	n_estimator = the number of decision trees max_depth=max depth of each decision tree
SVM	C: The penalty coefficient C of the objective function is used to balance the classification margin and misdivided samples, default C = 1.0 γ: Kernel coefficients, default γ= 1 / n_features

The choice of the size of the training set is an essential prerequisite for training the model, and therefore, the performance of the three models was tested on four different numbers of datasets: the number of training sets was set at 500, 5,000, 50,000, and 100,000. All data features were balanced, ensuring an equal number of snow pixels and non-snow pixels, effectively dividing the snow and non-snow samples equally. Exploring the sensitivity of the dataset size serves as a means to determine the most suitable dataset for optimizing the efficiency of the training process.

K-fold cross-validation was utilized to examine the different performance when using different sample sizes, as shown in Figure 4.4. This approach is a common practice for evaluating models using validation data. It involves partitioning the training dataset into K groups, known as "k-folds." Each fold serves as a test fold, while the remaining K-1 folds are utilized as the training set. Consequently, K models are created and individually evaluated on their performance against the testing set. The outcomes, typically measured using the Mean Squared Error (MSE), are then averaged to calculate the cross-validation error. Cross-validation is a strategic approach to maximize the use of limited data and provides evaluation

results closely resembling the model's performance on an independent test set (Chen et al., 2023; Karaca et al., 2022). Hence, 10-fold cross-validation was employed for the preliminary assessment of ML models.

Figure 4. 4 Theory of 10-fold validation (Image from Karl Rosaen Log http://karlrosaen.com/ml/learning-log/2016-06-20/)

The hyperparameter tunning and cross validation of LR, SVM and RF were implemented based on frequencies 6, 10, 18, 23, 36, 89 GHz in both horizontal and vertical polarizations. In addition, some ML can rank the importance of input variables such as RF, and then analyze which variables have the most influence on the model and explore how they relate to physical properties. The importance rank approach used was based on RF, named permutation feature importance. The theory of this algorithm lies in the concept of measuring the reduction in a model's performance score when a single feature value is randomly rearranged. This technique effectively severs the connection between the feature and the target variable. Consequently, the decline in the model's performance score provides insight into the extent to which the model relies on that particular feature.

4.1.3.2 Evaluation of SCA

The testing dataset from 2012 and 2022, was used to examine the model's prediction performance. The Tb data for those years were fed into the trained model to make predictions, and the predicted results were compared with the reference (MODIS) binary SCA values of those pixels. When evaluating the estimation performance of ML models on SCA, the confusion matrix shown in the table is used to define the accuracy of the predicted snow map. TP, FP, FN, and TN represent the number of snow-covered or snow-free pixels recorded under specific conditions. TP stands for true positives, which means both the reference data and predicted results are snow pixels. FP represents false positives, indicating that snow-free pixels were predicted as snow pixels. FN is for false negatives, indicating that both the reference data and predicted results are snow-free pixels, and TN represents true negatives, which represent that the snow pixels were predicted as snow-free pixels. Accuracy (the proportion of the total number of correct predictions), the recall rate (the proportion of snow that the model can capture), and precision (the proportion of all the estimated snow at all the real points) were used to calculate the F1 score (the harmonic average of precision and recall). The four parameters shown in Table 4.5 were calculated to validate the SCA. In addition, the ROC curve (Receiver Operating Characteristic Curve) and AUC (Area under the curve) value will be used for auxiliary analysis. The x-axis of the ROC curve presents FP, and the y-axis represents TP. The ROC curve illustrates how the classifier's performance evolves as the classifier's threshold is altered. An important feature of the ROC curve is its area (AUC), which is the area under the ROC curve. The larger the area, the better the performance of the classifier.

Table 4. 5 The confusion matrix quantifies the accuracy of the predicted snow cover map concerning the observed in situ snow cover. The terms TP, FP, FN, and TN denote the counts of snow-covered or snow-free observations under specific conditions.

Ground Observation	**Prediction**	
	Snow-covered (Positive)	Snow-free (Negative)
Snow-covered (Positive)	TP (True Positive)	FP (False Positive)
Snow-free (Negative)	FN (False Negative)	TN (True Negative)
Overall accuracy (OA)=(TP+TN)/(TP+TN+FN+FP) Recall=TP/(TP+FN) Precision = TP/(TP+FP) F1= (2*Precision *Recall)/ (Precision + Recall)		

4.1.3.3 Comparison with CMC analysis snow depth data

The CMC-modeled snow depth data were utilized for comparison with the RF-derived SCA. In Kelly et al.'s (2003) study, they highlighted that PMW sensors can detect snow when the snow depth exceeds 3 cm, but it remains subject to uncertainties. Consequently, the sensitivity analysis incorporated thresholds spanning from 1 cm to 10 cm for the conversion of ground snow depth measurements into corresponding snow cover or no snow information. The assessment method also encompassed the calculation of the confusion matrix, as outlined in Table 4.5.

Chapter 5

Result Analysis

5.1 Pre-setting of ML models

The validation data were used to examine the sensitivity of hyperparameters in different models. Subsequently, the parameters that resulted in the highest model accuracy were selected to optimize the models. Table 5.1 shows the final parameter selections obtained via GridSearchCV for each model.

Table 5. 1 The parameter selection of each model

Model	Parameter
LR	Solver: 'newton-cg', C=10
RF	n_estimator = 100; max_depth=8
SVM	C=10, Gamma= 1 / number of features (1/12)

Figure 5.1 illustrates the mean ROC curve and mean AUC values obtained through ten-fold cross-validation across three machine learning methods. A higher AUC is indicative of superior performance. Notably, as the sample size increased, the AUC of SVM also increased, but it consistently performed worse compared to LR and RF. The superior performance of LR over SVM suggests a preference for linear models (LR) over hyperplane-based models (SVM) in this dataset. LR demonstrated a slight drop in performance with larger sample sizes but stabilized. Despite achieving the highest accuracy of 0.88 with a sample size of 500, it is essential to recognize that a small sample size can elevate the risk of overfitting. Overfitting occurs when a model becomes overly sensitive to noise in the training data, diminishing its ability to generalize to new and unseen data. Consequently, a larger sample size is often favored, acknowledging the trade-off between accuracy and the risk of overfitting.

On the other hand, RF exhibited a mean AUC of 0.89 with a sample size of 50,000, maintaining this level with larger samples. Despite the strong performance of linear models, RF, as a highly flexible algorithm capable of capturing complex relationships and interactions between features, proved less prone to overfitting compared to LR. The comparison of ROC and AUC values across the three models favored RF, leading to its selection for further model

training. Considering the model's sensitivity to sample size and the need to balance accuracy with computational efficiency, the choice of 50,000 samples emerged as a judicious compromise. This decision aligns with the understanding that a moderately larger sample size enhances the model's ability to discern representative patterns without succumbing to computational challenges associated with excessively large datasets. Consequently, for the optimal balance between accuracy and computational efficiency, 50,000 samples were deemed suitable for subsequent model training.

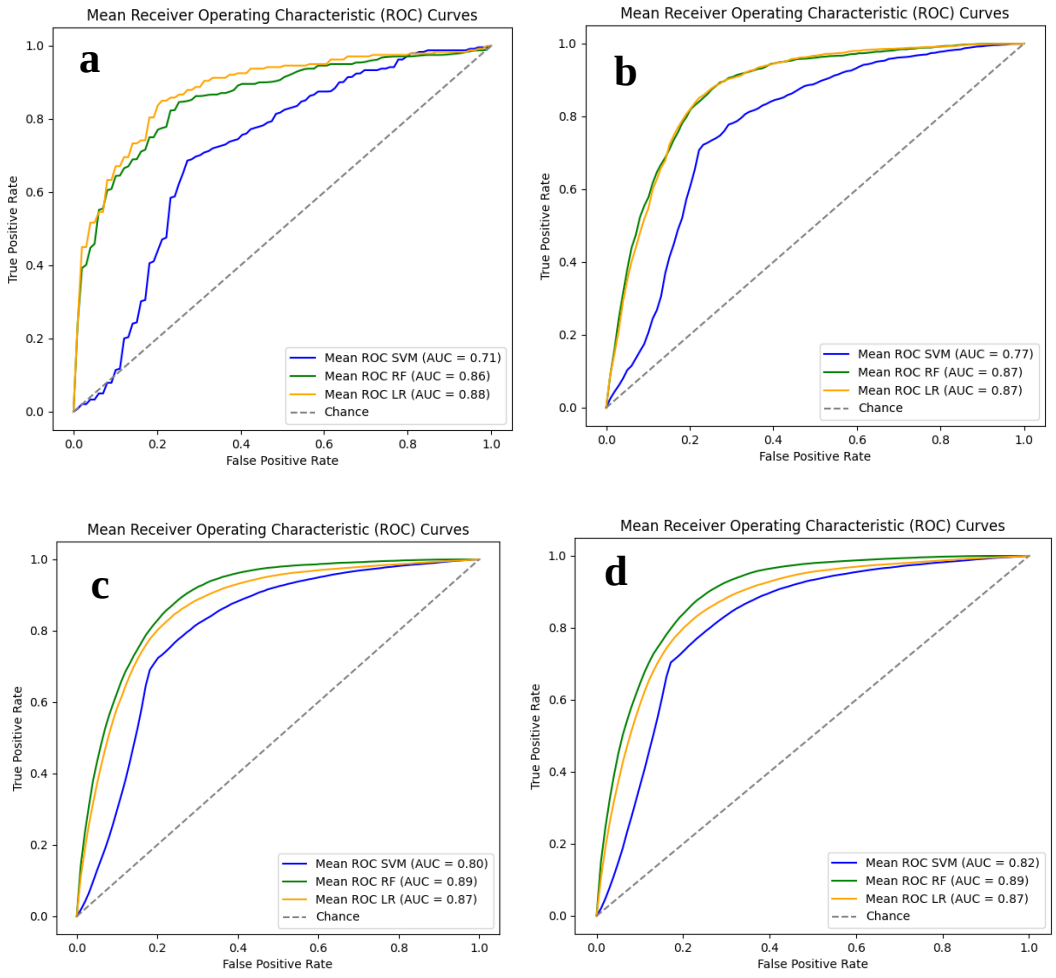

Figure 5. 1. Mean ROC and AUC for LR, RF and SVM models with varying sample sizes (a: sample size 500, b:sample size 5000, c: sample size:50000, d:sample size 10000) The graphs show the mean ROC curve for ten folds. Also shown is the line of chance.

Figure 5.2 is the visualization of the RF model, the maximum depth is 16 of the trained model, but since the tree is too crowd, so only display a DC with two depths as example. The decision tree begins with a root node splitting the dataset based on the condition (89V<=245.1), resulting in a relatively impure node (Gini impurity = 0.5) with 350 samples, roughly evenly distributed between the "Snow" and "Snow-Free" classes. The subsequent depth introduces two branches: the left branch (36H <=212.9)) with reduced impurity (Gini = 0.396) and a majority of 210 samples classified as "Snow-Free," and the right branch (36V <=254.05) with further reduced impurity (Gini = 0.255) and a majority of 140 samples classified as "Snow." The hierarchical arrangement of this tree signifies a systematic decision-making process designed to categorize instances according to particular conditions, enhancing the clarity of nodes with each subsequent division. Consequently, the classification of a given instance is established by tracing its route from the root to a distinct leaf node, guided by the fulfilled conditions. These leaf nodes serve as conclusive points for classification, and the class assigned to the designated leaf node serves as the predicted class for the instance. In the case of the RF classification model, it harnesses the combined decision-making of numerous trees via a majority voting mechanism, culminating in a robust and accurate prediction for each instance within the dataset.

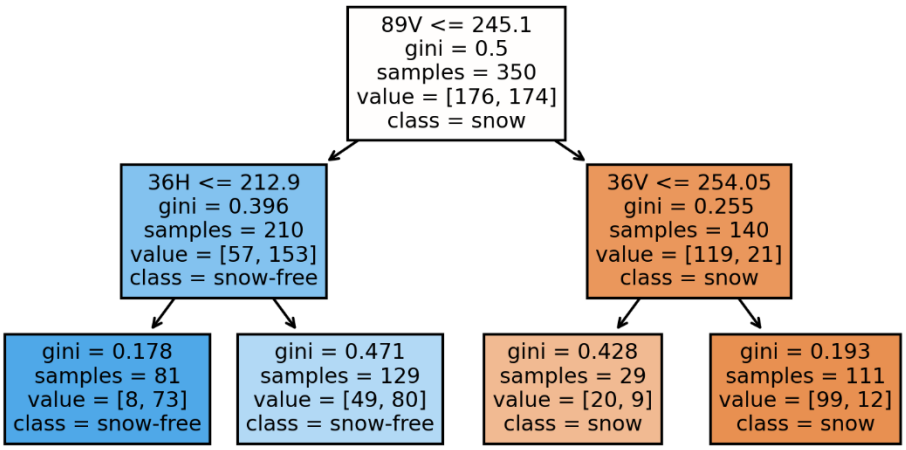

Figure 5. 2 The visualization of one decision tree example with tree depths=2

5.2 Evaluation results analysis

5.2.1 RF with different combinations of channels

To assess the varying performance of RF under different input channels, three combinations of channels were employed for AMSR-E/2 data: the first utilized all the relative channels and Tb differences specified in Grody & Basist's algorithm (1996) (18V-36V, 23V-89V, 23V, 18V-18H, 36V-89V, totaling five channels); the second incorporated all channels from SSM/I (18H/V, 23V, 36H/V, and 89H/V, totaling eight channels); while the third encompassed all 12 available channels of AMSR-E/2 (6H/V, 10H/V, 23H/V, 36H/V, and 89H/V). The results in Table 5.2 indicate that the RF model based on all channels outperforms those based on only five or eight channels. The addition of Tb differences to the model is found to be less effective than single-frequency Tb, as Tb differences provide relatively less information, and ML can extract more valuable information from individual Tb frequencies. By comparing the impact of different input channels on the accuracy of the RF model, it becomes evident that increasing the number of parameters enhances the model's ability to capture the relationship between snow cover and Tb values. The inclusion of 06H/V and 10H/V channels as input parameters leads to a slight improvement in model accuracy, suggesting that low-frequency bands play a role in snow identification.

Table 5. 2. RF performance on evaluation dataset using three different channel combinations

	Grody and Basist's algorithm (1996) related channels	All channels of SSM/I	All channels of AMSR-E/2
Accuracy	0.709	0.841	0.860

The next step involves a more in-depth examination of the significance of these 12 channels in the model's performance. Figure 5.3 illustrates the sorted feature importance (permutation) from the ML model. This approach was conducted with ten repetitions, so the

x-axis values represent average values divided by ten. High permutation importance indicates that variables have a more substantial impact on the model's performance.

Among the frequencies, 36 GHz stood out prominently in the model, followed closely by 6 GHz and 89 GHz. Both 89 GHz and 36 GHz are crucial frequencies for snow identification, as outlined in Grody and Basist's algorithm (1996). Higher frequencies, like 89 GHz, exhibit sensitivity to volume scattering near the surface, making them suitable for detecting shallow snow cover with weaker scattering characteristics. However, 89 GHz is significantly affected by clouds and scatters more in rainy and non-snow conditions. Consequently, the utilization of 36 GHz and 89 GHz is essential for global snow cover identification, explaining their significance in the figure. Compared to the SSM/I sensor, the AMSR-E/2 sensor includes two additional low-frequency bands, 6 GHz and 10 GHz. The figure reveals that 6 GHz is nearly as important as 36 GHz in the model, while 10 GHz horizontal didn't rank as high, though 10 GHz vertical proved slightly more significant than 18 GHz. 10 GHz can provide more information about snow in forested areas (Tong et al., 2010). The low-frequency band can be valuable in determining snow conditions or the state of the ground surface under snow cover, with frozen soil influencing microwave radiation and introducing uncertainties in snow detection (Tsutsui & Koike, 2012). Thus, 06 GHz plays a crucial role in areas with snow cover and frozen soil. In terms of the 23 GHz channels, 23 GHz vertical ranked higher than 23 GHz horizontal, as 23 GHz vertical exhibits sensitivity to water vapor, which is useful for identifying precipitation. An additional empirical analysis was conducted, focusing on training the model exclusively using the first four frequencies considered crucial. The obtained results showed comparable performance to the comprehensive twelve-channel approach. Despite this similarity, the decision was made to opt for utilizing all twelve channels in the model training. This decision is grounded in the acknowledgment that each frequency contributes valuable information, and the inclusion of all channels augments the model's overall ability to capture intricate patterns associated with snow detection. This choice is aimed at providing a more comprehensive and robust approach to the task.

Overall, the above explanations regarding the importance rankings align with the facts of snow retrieval using PMW methods. Although ML approaches lack physical information and rely heavily on the quality of input datasets, the sorting of importance in the RF model demonstrates a correlation between data-driven and physically derived results, and such analyses enhance the interpretability of ML.

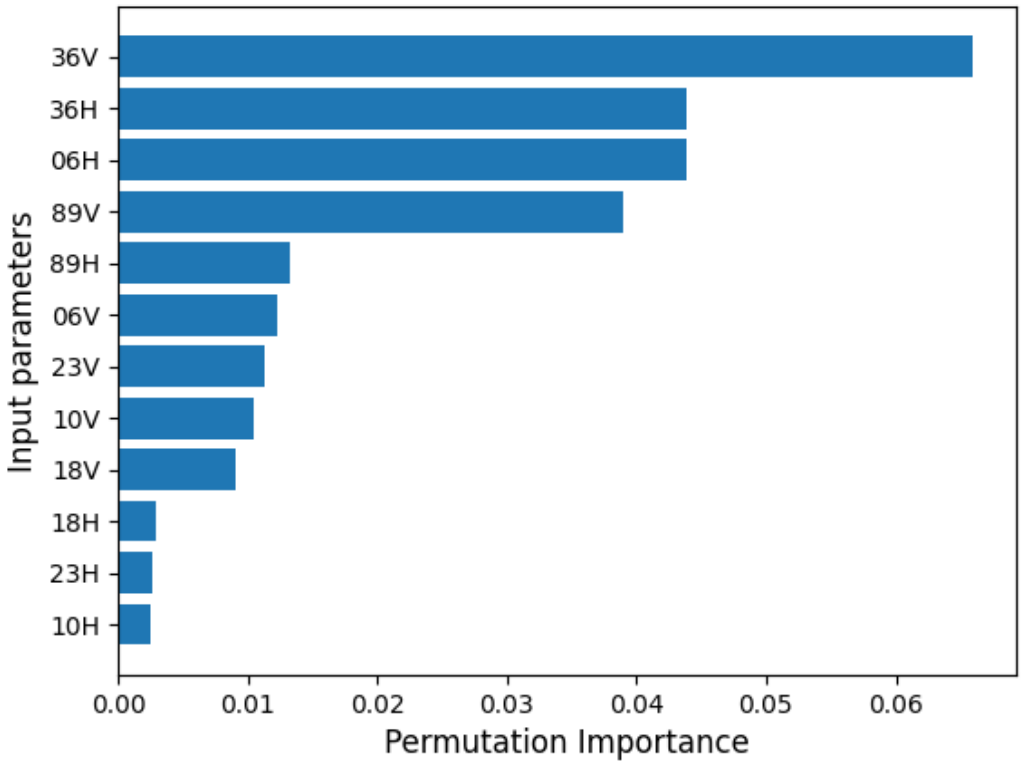

Figure 5. 3 The permutation importance of input parameters

5.2.2 General evaluation on snow detection

Figure 5.4 displays the performance of RF on snow detection for different months using testing data. In Oct, the recall and F1 were the lowest, but accuracy was the highest. The high accuracy primarily resulted from the correct classification of non-snow pixels, as there was less snow presence in Oct. Generally, for both models, recall was consistently higher than precision in Dec and Feb, while Oct and Apr showed the opposite results. A high recall and

low precision mean that the snow cover area was more likely to be overestimated than underestimated. As a result, a low recall rate in these months suggests that much snow was missed by the RF model. In large datasets, recall and precision often have a trade-off relationship. Ideally, both indexes should be high, but in practice, when precision is high, recall tends to be low, and vice versa.

The Arctic cold period can be categorized into five stages: early snow, early cold, deep cold, late cold, and thaw. In the context of this study, Oct marks the onset of snow cover, Dec represents the development of deep hoar, Feb still falls within the period of deep hoar development, and by Apr, the ground freezing has concluded, and the snow has melted. Dec and Feb exhibited lower precision, suggesting a prevalence of overestimations in predicted snow cover. Depth hoar emerges as the predominant factor contributing to these overestimations. Depth hoar is known to develop in high Arctic regions with shallow seasonal snowpacks exposed to extended cold temperatures, leading to a significant temperature differential between the relatively warm ground (Giddings & LaChapelle, 1962). The increase in depth hoar grain size leads to more significant scattering, subsequently resulting in reduced snowpack emissivity (Foster et al., 1984). Furthermore, microwave brightness temperature (Tb) decreases with increasing depth hoar thickness (Hall et al., 1986).

Oct and Apr displayed lower recall compared to precision, implying a higher tendency for underestimating snow cover in these months. In Oct, the snow depth is shallow, which may not sufficiently reflect strong snow emission, contributing to the underestimations. In April, the already melted snow cover and increased water content may lead to elevated Tb values, causing underestimations. The evaluation results indicate that the performance of the RF model varies for estimating snow cover during different months due to the seasonal cycles of snow.

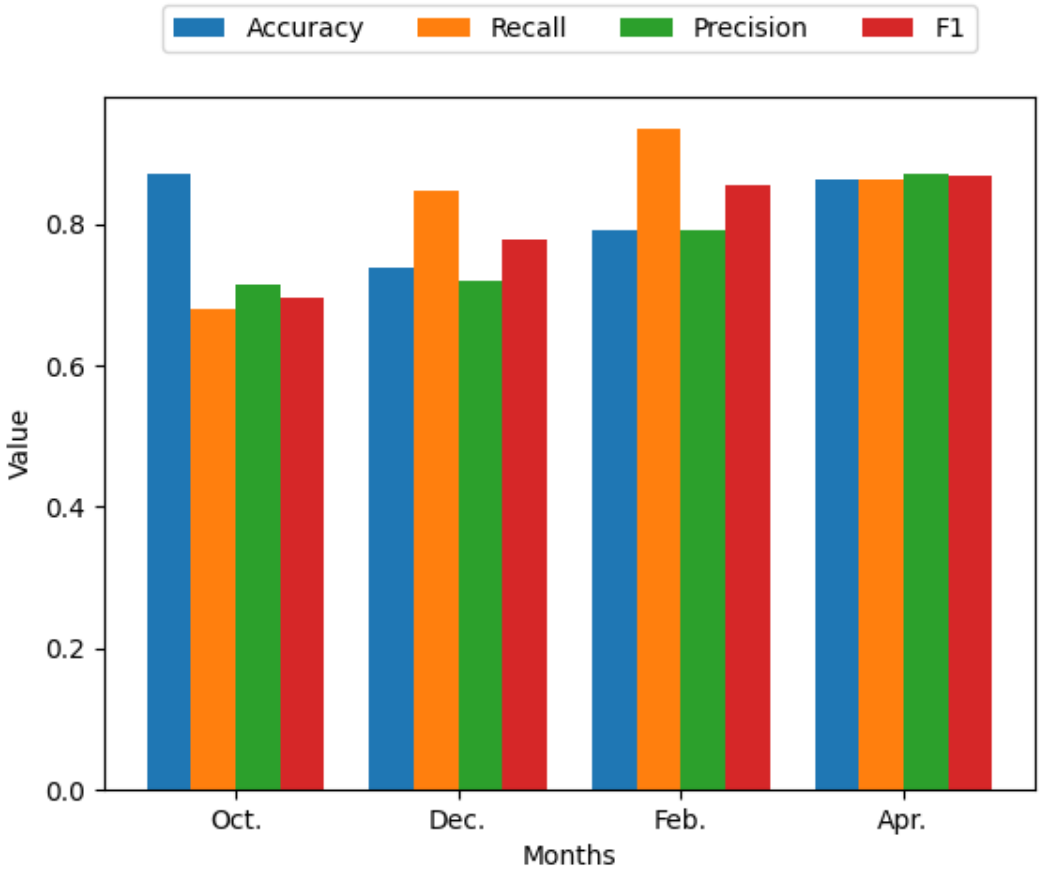

Figure 5. 4 Performance of RF model for four months.

Snow in different environment has specific characteristic which could result in the different performance of RF. At the beginning of the accumulation, snow primarily consists of tundra snow at low latitudes, and it later appears as taiga snow, alpine snow, and a small amount of prairie snow. Figure 5.5 presents the results of two retrieval methods for four snow classes. These four snow classes were selected since this study focused on the areas with more snow, including tundra, taiga, prairie, and alpine. The retrieval models for the prairie class achieved the highest accuracy. This is because accuracy calculations depend on the number of snow pixels and non-snow pixels. The number of TP and FN, which are part of the calculation formula, significantly affects the overall accuracy. If the number of FN is predominant, higher accuracy can be achieved even if TP is small. The prairie snow region has the least snow among the analyzed snow environments. Therefore, in these four months, most of the prairie snow

was not observed under PMW and MODIS, resulting in higher overall accuracy compared to other snow environments. In contrast, the alpine type performed the worst in all four evaluation parameters. This is because alpine snow is complex terrain that is subjected to winds, leading to more complex snow stratigraphic structure and texture (Sturm et al., 1995). Tundra snow consistently showed the highest recall, precision, and F1, indicating that over 90% of snow pixels can be identified by the ML models, and over 80% of covered pixels exist in the predicted snow cover in the tundra area. Tundra snow is typically found above or north of the tree line and has rare melt features, resulting in stable snow cover over the four months compared to other snow classes. Taiga snow, although less accurate than tundra and prairie snow due to forest density, performed better than alpine snow.

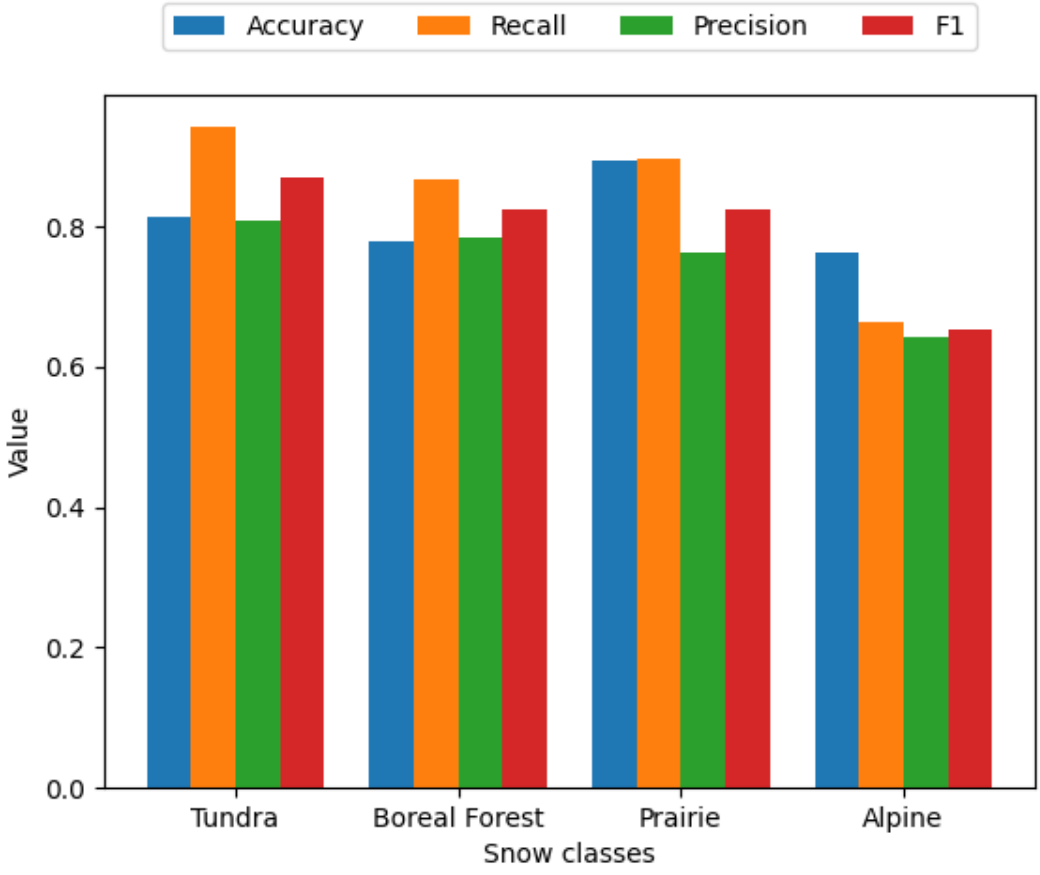

Figure 5. 5 Performance of RF model for four snow classes.

5.2.3 Estimating SCA map using PMW Tbs and MODIS SCA product trained model

The above analysis aimed to detect the relationship between ML's ability in snow detection and the month and snow environment. The following assessment focused on how the distribution of the RF-SCA differs from that of MODIS-SCA and PMW-SCA. The daily SCA was estimated using the RF model and compared it to PMW-SCA and MODIS-SCA. Figures 5.6-5.9 display the spatial distribution patterns of snow cover on the 15th of Oct 2018, Dec 2018, Feb 2019, and Apr 2019, including PMW snow cover estimated by the Grody and Basist's algorithm (1996), MODIS snow cover, and the snow cover estimated by the RF model. In the ML implementation, pixels with a CPC greater than seven days were removed to improve dataset accuracy. However, there was a classification of clouds in those maps to depict the day's appearance more accurately, and the night area was also marked.

From the graphs, it is evident that the spatial distribution of PMW-SCA and MODIS-SCA is relatively consistent. The primary differences between PMW-SCA and MODIS-SCA are concentrated in the northeastern Arctic (highlighted by the red circle) and in small parts of North America (highlighted by green circle 1), as well as the region of western Russia near Finland (highlighted by green circle 2). The marked regions are only presented in Figure 5.6a, but they are the common areas for analysis in Figures 5.6 to 5.8.

In comparison to PMW-SCA and MODIS-SCA, the areas within the red circles are where PMW tends to overestimate snow cover. These regions, located in the high-altitude tundra, are strongly affected by depth hoar and frozen soil, causing PMW to detect lower Tb values and misidentify them as snow. The green circles are mainly situated in the densely forested taiga region, which obstructs the snow signal, resulting in the underestimation of PMW. Additionally, the topography of the taiga region exhibits significant variability contributing to errors.

The RF-SCA, estimated by the trained model based on the reference MODIS-SCA, was expected to bring about two main improvements. Firstly, it was anticipated to reduce the number of pixels that overestimated SCA compared to MODIS, represented by 'POM' (PMW overestimated than MODIS, as indicated by the red circle). Secondly, it was expected to

increase the number of pixels that underestimated SCA compared to MODIS, labeled as 'PUM' (PMW underestimated than MODIS, represented by the green circle in the figures). As observed in these figures, the 'POM' area experienced a significant improvement with the RF model, whereas the 'PUM' area showed relatively less change. Furthermore, the RF-SCA effectively fills in the MODIS night area based on the Tb values provided by PMW."

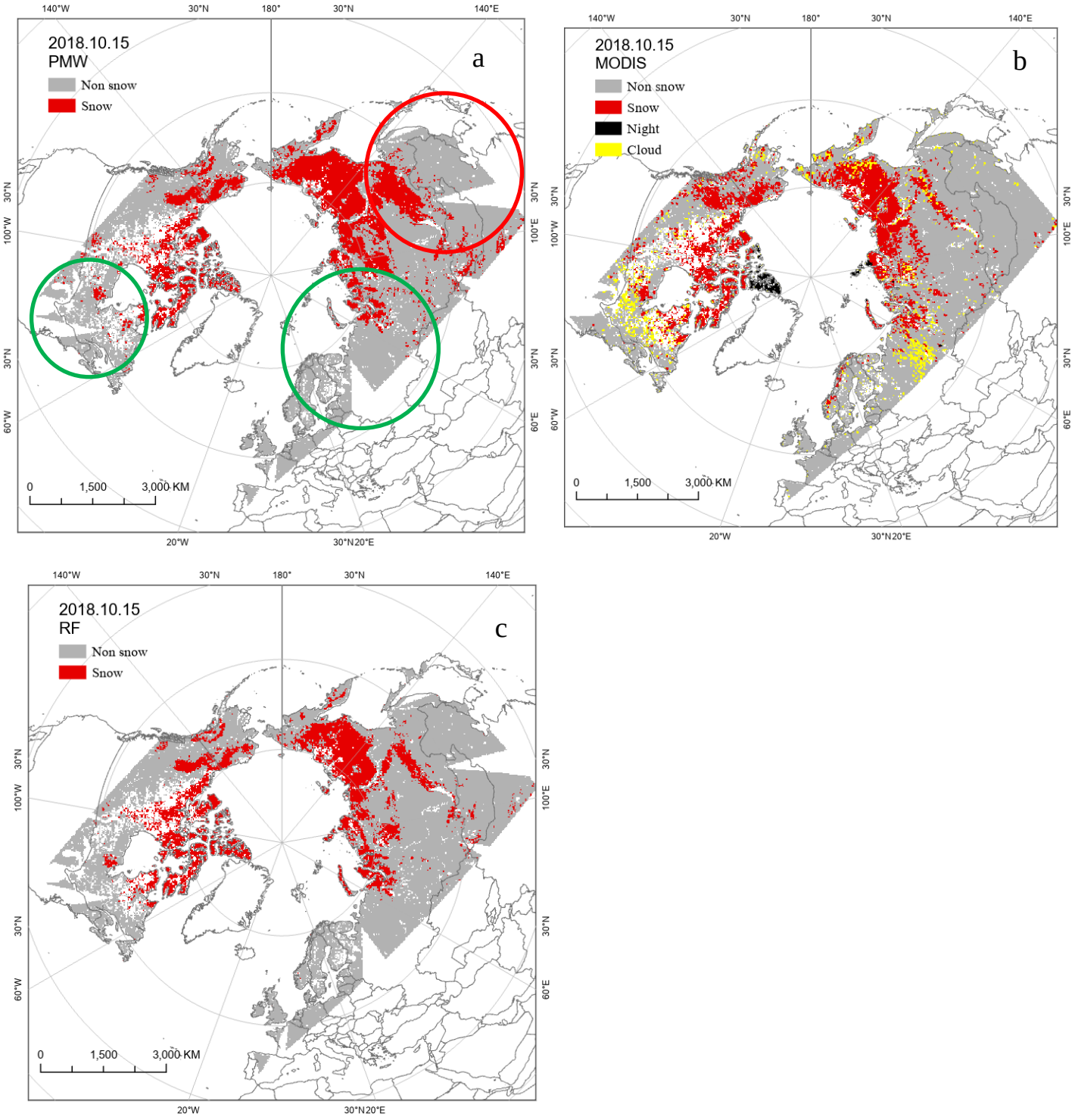

Figure 5. 6. Spatial distribution of SCA of Oct. 15, 2018, derived from three algorithms. a) PMW derived SCA based on Grody and Basist's algorithm (1996), b) MODIS derived SCA, c) RF derived SCA; Red circle: 'POM' area; Green circle: 'PUM' area

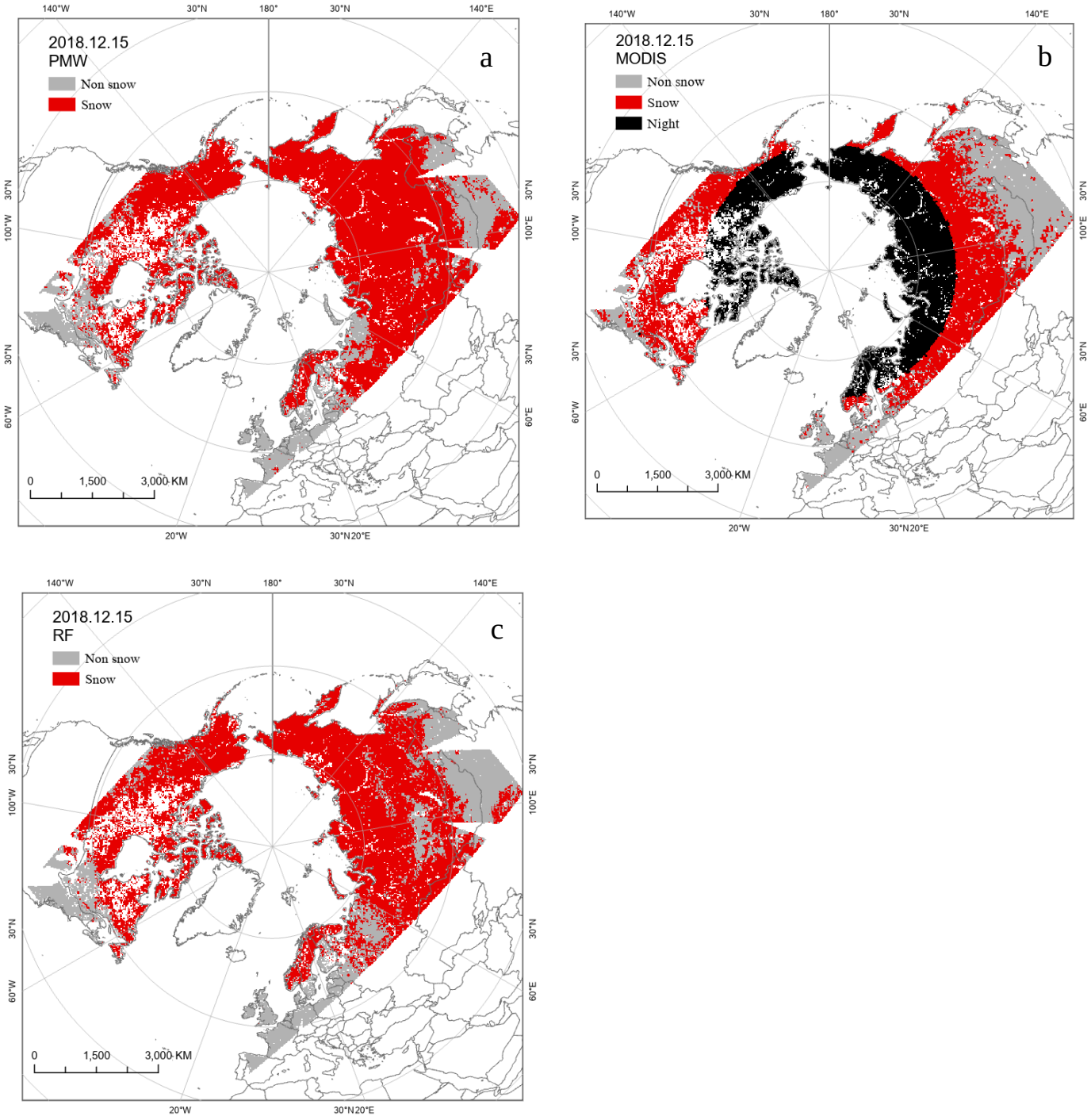

Figure 5. 7 Spatial distribution of SCA of Dec. 15, 2018, derived from three algorithms. a) PMW derived SCA based on Grody and Basist's algorithm (1996), b) MODIS derived SCA, c) RF derived SCA

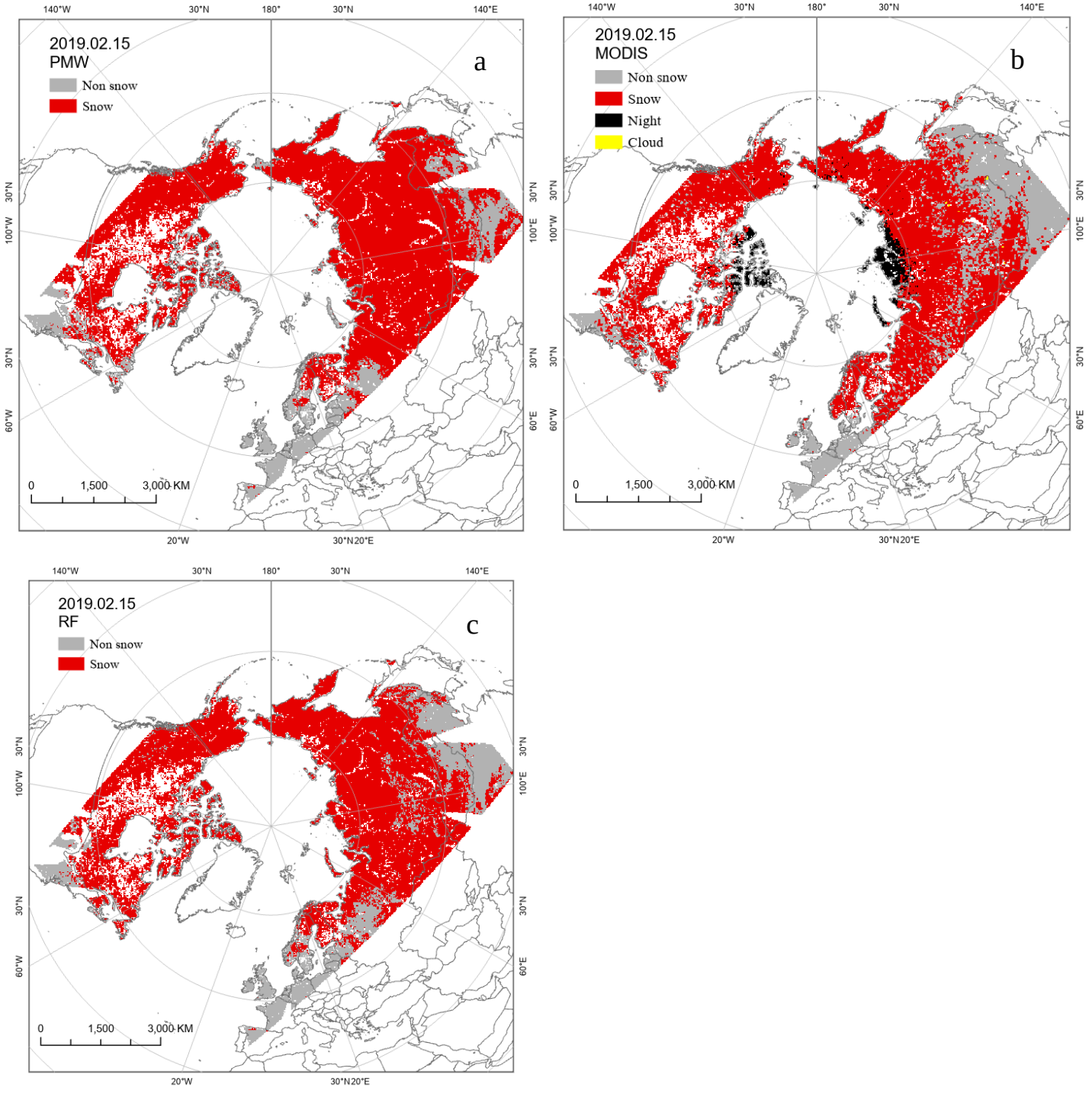

Figure 5. 8 Spatial distribution of SCA of Feb. 15, 2019, derived from three algorithms. a) PMW derived SCA based on Grody and Basist's algorithm (1996), b) MODIS derived SCA, c) RF derived SCA

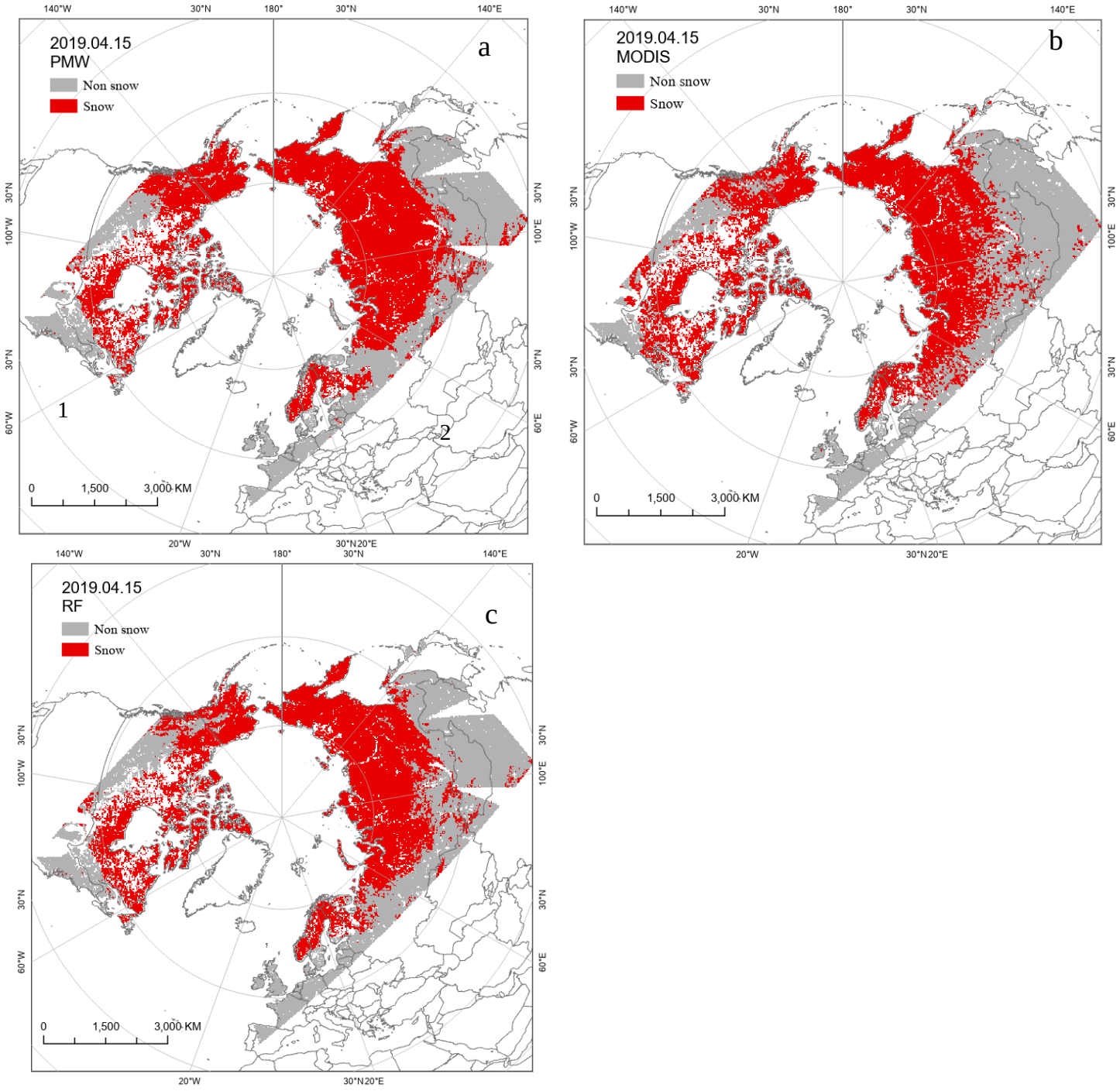

Figure 5. 9 Spatial distribution of SCA of Apr. 15, 2019, derived from three algorithms. a) PMW derived SCA based on Grody and Basist's algorithm (1996), b) MODIS derived SCA, c) RF derived SCA

Table 5.3 provides a detailed analysis of performance metrics in snow cover area estimation, contrasting MODIS-SCA reference data with two distinct methodologies—PMW-SCA and RF-SCA—across different months (Oct, Dec, Feb, and Apr). The monthly means are also presented. Notably, the rise in precision signifies a reduction in the 'POM' area, demonstrating an improved ability to precisely identify snow-covered regions. Conversely, a marginal decrease in recall indicates that the 'PUM' area remains relatively consistent. The mean results align with the spatial distribution analysis, revealing that RF-SCA leads to increased precision by refining the delineation of 'POM' areas, while 'PUM' areas show limited improvement. Across various metrics (overall accuracy, precision, and F1) and months, RF-SCA consistently outperforms PMW SCA, emphasizing its effectiveness in snow cover estimation. This comprehensive examination affirms RF-SCA as a robust and preferable methodology for accurate snow cover assessments.

Table 5. 3 Comparative analysis of SCA estimation performance metrics between reference data (MODIS-SCA), and evaluation data (PMW-SCA, RF-SCA) for different months and their monthly averages.

		Evaluation data									
		Oct		Dec		Feb		Apr		Mean	
	Reference data	PMW-SCA	RF-SCA	PMW-SCA	RF-SCA	PMW-SCA	RF-SCA	PMW-SCA	RF-SCA	PMW-SCA	RF-SCA
Accuracy	**MODIS-SCA**	0.838	0.881	0.717	0.758	0.721	0.785	0.824	0.868	0.775	0.823
Recall	**MODIS-SCA**	0.697	0.657	0.838	0.784	0.933	0.923	0.888	0.876	0.839	0.810
Precision	**MODIS-SCA**	0.601	0.762	0.66	0.743	0.706	0.77	0.782	0.857	0.687	0.783
F1	**MODIS-SCA**	0.645	0.704	0.739	0.763	0.804	0.84	0.831	0.866	0.755	0.793

5.2.4 Analysis of Tb character in ‘POM’ and ‘PUM’ area

Building upon the results presented earlier, further analysis was conducted to investigate the factors contributing to RF's enhancement of the 'POM' and 'PUM' areas. Firstly, box plots depicting the Tb characteristics of each pixel type for each month were created (as shown in Figure 5.10). Using 18GHz_V, 23GHz_V, 36GHz_V, and 89GHz_V as examples, the four boxes represent Tb values for different conditions: both snow, both non-snow, ‘POM’ and ‘PUM’. The black line in the middle represents the median value of the data, and the width of the box encompasses the data falling between the 25th and 75th percentiles, indicating the range of values from lower to higher.

Generally, the relationships between the four types of pixels were similar across the four months. The Tb value of 'PUM' was consistently low and close to that of 'non-snow,' while 'POM' was closer to the Tb values of 'snow.' As the frequency increased, the separability between the four classes also increased. Throughout each snow season, spanning from Oct to Apr of the following year, the snow underwent three stages: accumulation, stabilization, and ablation. The mean Tb value of 'non-snow' and 'PUM' remained relatively stable over the four months, while 'POM' exhibited a decrease in Tb value from Oct to Feb and a slight increase in Apr.

A critical factor for snow detection based on Tb is the Tb difference between low frequency and high frequency. The purple box in the figure represents the Tb values of the 'PUM' region, which is why the threshold values for low frequency and high frequency were relatively close, such as 18GHz_V and 36GHz_V, and 36GHz_V and 89GHz_V. Grody and Basist's algorithm (1996) cannot recognize points in the 'PUM' region as snow due to the minimal difference between low and high frequencies. However, for the 'POM' region, the Tb values of some non-snow points changed under the influence of the environment, causing them to meet the conditions for being recognized as snow. The results of RF-SCA showed that the 'POM' area was more easily improved than the 'PUM' area. Subsequent sections will provide a more specific analysis of the reasons for this.

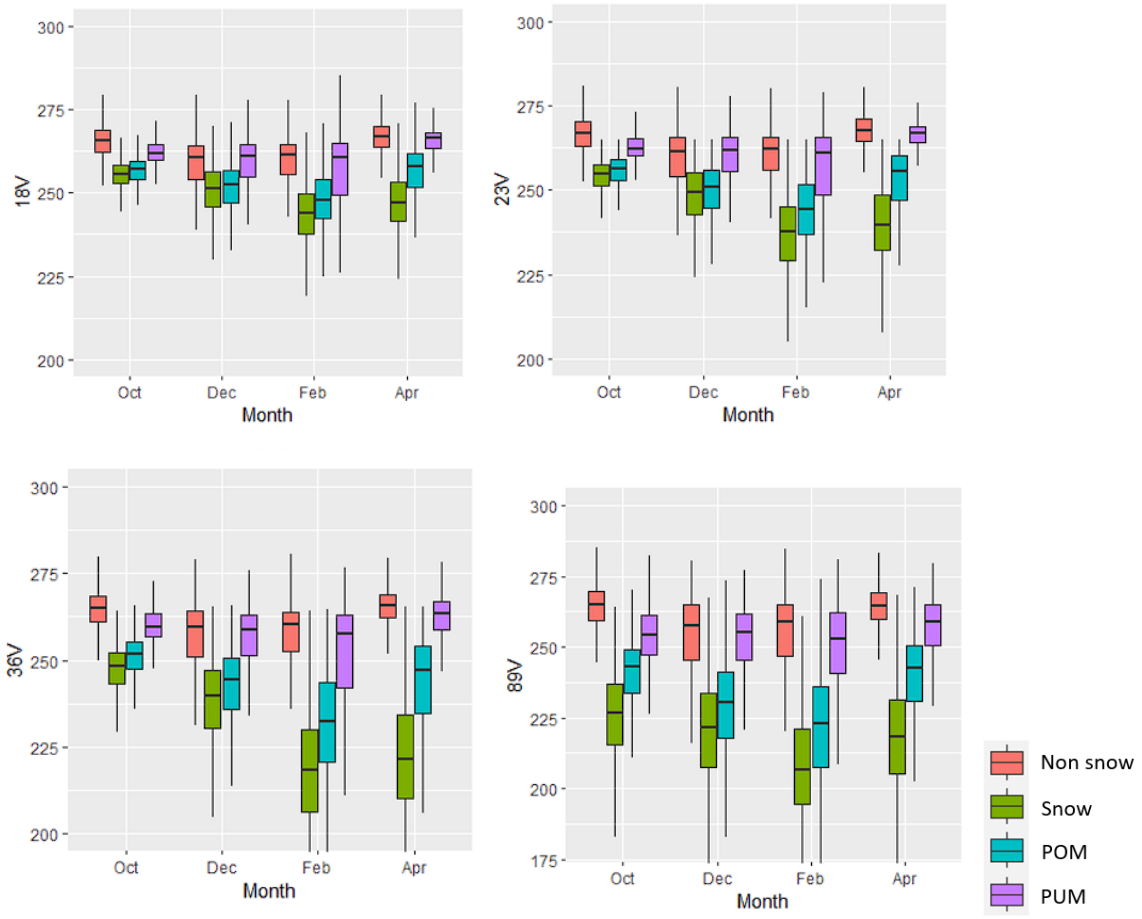

Figure 5. 10 Variability of Tb values by frequency for the four periods of study.

5.2.5 Analysis of errors and improvements in 'POM' area

Based on the previously described snow distribution, a detailed explanation was provided from several perspectives. In contrast to PMW-SCA and MODIS-SCA, the 'POM' region was consistently observed between 60°E and 140°E in Eurasia (highlighted by the red circle) throughout all four months. These areas encompass high plateaus such as Mongolia and southeastern Russia, although the Tibetan Plateau was not included in the study area. According to research conducted by Tsutsui & Koike (2012), biomass emissions under snow can influence microwave signals, leading to inaccuracies in snow estimates. In high-altitude plateau areas, frozen soil is often present beneath the snow cover, and the dielectric properties of frozen soil are similar to those of a dry snowpack. As a result, microwave satellite sensor

data from frozen ground can be erroneously interpreted as a dry snowpack, leading to overestimations of snow cover.

ML redefines the categories of these points based on the MODIS reference data, enabling the discovery of new Tb features that yield improved results. This leads to a significant enhancement in RF-based snow estimates for this region, resulting in reduced snow cover compared to the original PMW SCA, making it more consistent with MODIS SCA.

5.2.6 Analysis of errors and improvement in 'PUM' area

The snow pixels that were underestimated ('PUM') by PMW compared to MODIS were classified in the algorithm as non-scatterers or other types of scatterers. PMW-SCA was underestimated compared to MODIS-SCA because it was identified as precipitation, frozen ground, or cold deserts in the decision tree algorithm. The daily count of these identified scatterers was accumulated and averaged over a month to obtain the 'PUM' attribute for each month over a ten-year period. To illustrate the complete temporal analysis, the entire dataset range was used.

In Figure 5.11, the proportion of each scattering material for each month is depicted. Since scatterers were identified individually, and some Tb characteristics of a pixel could meet the conditions for more than one type of scatterer, such as when one pixel was identified as both precipitation and frozen ground, it was counted in both of these categories for that day. Consequently, the total percentage for these four types exceeded 100%. When examining the time series, the proportion fluctuation of non-scattering materials and frozen pixel amounts remained relatively stable, particularly when compared to precipitation and cold deserts. In Feb, precipitation and cold deserts displayed opposing changes (precipitation decreased while cold deserts increased) due to temperature influences. For each individual month, the percentage of precipitation was significantly higher than that of other scatterers, exceeding 90% in Apr. Therefore, the identification of precipitation stands out as the most significant factor contributing to the underestimation of snow by PMW compared to MODIS.

The areas where PMW was underestimated pose a challenge for improvement in the RF model, and most of the Tb characteristics of these points indicate precipitation. Distinguishing between precipitation and wet snow in PMW data is difficult. However, the presence of water in snow does not affect snow monitoring by optical satellites. Even when PMW data is acquired at night, it still cannot completely avoid the impact of snow melting.

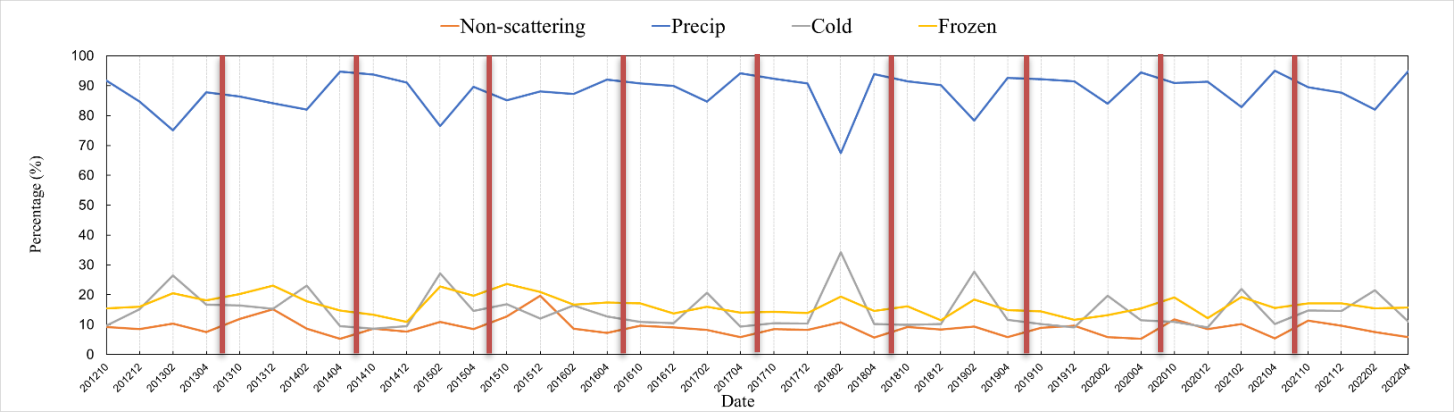

Figure 5. 11 The proportion of attributes of the average underestimated pixels for each month over the entire study period. Red vertical lines separate each year from the next.

The 'PUM' areas highlighted within the green circle are typically located in alpine snow regions characterized by high FF. While alpine snow doesn't receive as much precipitation as prairie snow, some liquid water may be produced by the melting of icicles within the canopy, and occasional warm periods during winter may result in liquid water formation (Sturm & Liston, 2021). This liquid water can refreeze within the snowpack, causing discrepancies in PMW data. Additionally, as noted in Vander Jagt's research (et al., 2013), FF values greater than 60% can mask virtually all microwave signals attributed to snow, often leading to underestimations by PMW in regions with high FF.

Nevertheless, in those regions, there was only a marginal improvement in accuracy after applying the RF model, or in some cases, a worsening of the results. This discrepancy could be attributed to incorrect data in the training set, such as inaccurate MODIS reference data in forested areas. Forests attenuate microwave signals from snow and affect snow's reflectivity. NDSI values decrease when other features are mixed in pixels or when snow is

shaded or under a forest canopy (Da Ronco et al., 2020). Consequently, in densely forested areas, lower NDSI values are typically observed, leading to the omission of snow pixels by MODIS (Poussin et al., 2023). Therefore, the accuracy of pixels in densely forested regions remains questionable, potentially resulting in limited improvement in the 'PUM' area.

5.3 Comparison with snow depth data

Previous research has indicated that PMW sensors can detect snow when the snow depth exceeds 3 cm (Kelly et al., 2003). The relationship between RF-SCA and CMC-SCA under different snow depth thresholds is illustrated in Figure 5.12, utilizing data from 2018 and 2019. Except for precision in Oct, changes in other accuracy metrics were less than 20% with increasing snow depth. This is because, as snow depth increases, recall values also increase in all four months. Considering the balance between all the accuracy indicators, 3 cm is reasonable to be selected as the snow depth threshold to identify the snow cover.

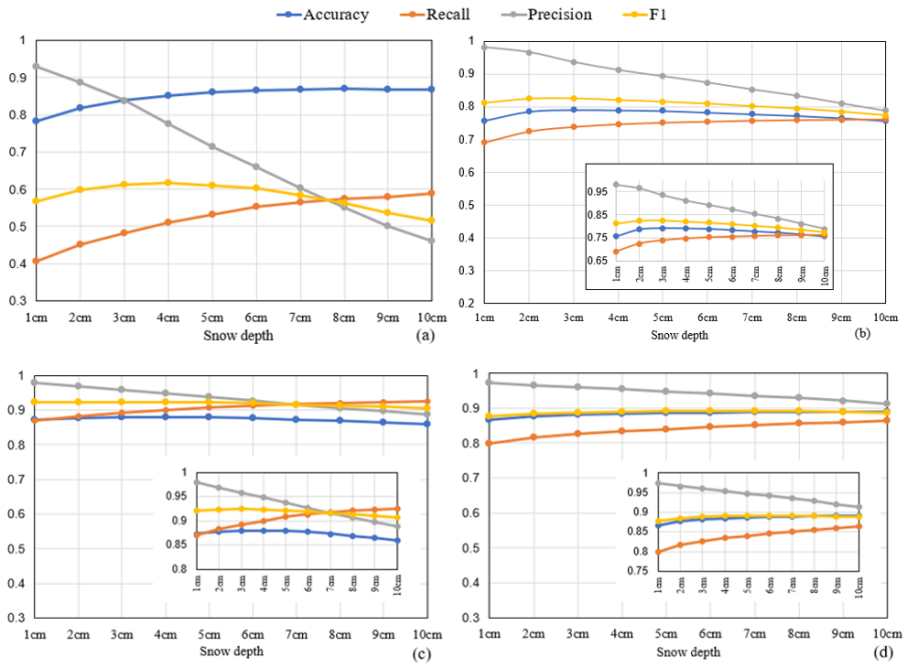

Figure 5. 12 Performance Evaluation of RF-SCA compared to CMC-SCA at various snow depths (a. Oct, b. Dec, c. Feb, d. Apr). The figure displays the accuracy metrics—overall accuracy, recall, precision, and F1 score—across different snow depth thresholds (1 to 10 cm).

The snow threshold of 3 cm is subsequently applied to the CMC snow depth dataset for each month to generate the corresponding snow map. Subsequently, the confusion matrix of PMW-SCA, MODIS-SCA, and RF-SCA is computed with the obtained CMC-SCA. The results presented in Table 5.4, reveal that the average precision between RF-SCA and CMC-SCA is close to 90%, with both average overall accuracy and average F1 exceeding 80%, while the average recall rate is relatively low, standing at less than 80%. The diminished recall is attributed to MODIS-SCA, serving as the reference data, exhibiting the lowest recall value, thereby impacting the results of RF-SCA despite PMW-SCA displaying the highest recall value. This underscores a noteworthy aspect, indicating that MODIS-SCA is more likely to missing points in comparison to CMC-SCA. However, it may also stem from the fact that CMC-SCA tends to overestimate compared to MODIS-SCA in certain regions, a phenomenon linked to the inherent uncertainty in interpolation results due to limited site data in Russia, making CMC data reliant on in-situ measurements and interpolation techniques. In terms of the precision, MODIS-SCA consistently outperformed PMW-SCA over the four months, indicating that MODIS-SCA had a lower classification error rate, while PMW-SCA had a lower classification miss rate. Despite disparities in consistency between PMW-SCA, MODIS-SCA, and CMC-SCA, the RF-SCA trained on Tb data and MODIS reference snow data, exhibited significant improvements compared to both MODIS-SCA and PMW-SCA. This observation underscores the advantages of leveraging machine learning models capable of integrating diverse input data sources and effectively discerning feature relationships.

		Evaluation data														
		Oct			Dec			Feb			Apr			Mean		
	Comparison data (reference data)	PMW-SCA	MODIS-SCA	RF-SCA	PMW-SCA	MODIS-SCA	RF-SCA	PMW-SCA	MODIS-SCA	RF-SCA	PMW-SCA	MODIS-SCA	RF-SCA	PMW-SCA	MODIS-SCA	RF-SCA
Accuracy	CMC-SCA	0.828	0.856	0.874	0.810	0.777	0.791	0.862	0.755	0.863	0.850	0.847	0.870	0.837	0.809	0.849
Recall	CMC-SCA	0.663	0.618	0.624	0.841	0.707	0.739	0.903	0.720	0.858	0.857	0.796	0.826	0.816	0.710	0.762
Precision	CMC-SCA	0.609	0.706	0.774	0.871	0.946	0.936	0.929	0.980	0.974	0.875	0.923	0.936	0.821	0.889	0.905
F1	CMC-SCA	0.635	0.659	0.691	0.856	0.809	0.826	0.916	0.830	0.912	0.866	0.855	0.877	0.818	0.788	0.827

Table 5. 4 Comparative analysis of SCA estimation performance metrics between reference data (CMC-SCA), and evaluation data (PMW-SCA, MODIS-SCA, RF-SCA) for different months and their monthly averages.

Chapter 6
Discussion and Conclusion

6.1 Main findings and limitations

This thesis investigates the application of various ML models for snow mapping utilizing PMW Tb data and MODIS binary snow data. The results show SVM perform the worst, then is LR, and the best is RF. Although LR had the highest AUC when using sample size 500, but a larger sample size is preferred because it can capture more information. Thus, 50000 was selected since RF had the highest AUC. Evaluation outcomes were influenced by different months and snow classes, revealing variations in snow characteristics across environments. PMW exhibited a tendency to detect more snow than MODIS in high-altitude, dry, and cold regions due to frozen ground influence, while densely forested areas experienced reduced snow detection. When estimating daily SCA, RF-SCA demonstrated improved precision but decreased recall, indicating reduced overestimation but minimal improvement in underestimation. Furthermore, RF-SCA exhibited better consistency compared to MODIS-SCA and PMW-SCA against CMC-SCA. The study underscores the nuanced influence of environmental factors on snow mapping results and highlights the potential of RF for accurate SCA estimation in diverse conditions.

While the application of the RF model for snow mapping based on Tb data and MODIS reference data has demonstrated success in capturing MODIS night areas and mitigating overestimation in high-altitude regions influenced by PMW, certain limitations should be acknowledged. Notably, the model exhibits less improvement in predicting SCA in ‘PUM’ areas, where misclassifications often arise due to precipitation interference. Addressing this challenge involves considering additional data to incorporate atmospheric state information, particularly for distinguishing between precipitation and wet snow in PMW data. The resampling of MODIS data to a coarser resolution, while necessary for compatibility with PMW data, poses a potential compromise to the accuracy of snow mapping. Furthermore, the dependency of MODIS SCA on NDSI and CPC thresholds poses a limitation, especially for local areas where snow identification criteria may require adjustment to align with specific

conditions. Additionally, the study recognizes the temporal disparities between MODIS daytime observations and Tb data acquired at night, further complicated by the temporal variability of the CGF product. The potential inconsistency in data acquisition times introduces uncertainties that may impact the precision of the analysis. Despite these limitations, the RF model has shown notable improvements, particularly in reducing overestimation in certain regions, contributing valuable insights to snow mapping methodologies. However, when considering the application of this technique to future PMW observations would require careful consideration of environmental similarities, potential adjustments for different sensor specifications, and continuous model adaptation to evolving technological advancements and observational capabilities.

6.2 Discussion of alignment with aims, objectives, and previous studies

In the assessment of ML models for snow detection utilizing PMW Tb data and MODIS observations, SVM was less effective than LR, which indicates the hyperplane-based model was not suitable for this dataset. SVM was the most time-consuming model among the three models. LR emerged as less effective than RF due to its assumptions of linearity and feature independence, which may inadequately capture the complexities of snow cover patterns. In contrast, RF provides computational efficiency and robustness, making it a practical preference for large-scale snow mapping applications. This observation aligns with the research findings, underscoring the importance of selecting models that balance computational efficiency and the intricacies of snow mapping datasets. The research further investigated disparities between satellite-derived snow, ML-derived snow combining optical and PMW observations, and station-measured snow. Results revealed that the ML-based approach, incorporating both PMW and MODIS data, outperformed methods relying solely on either data source for snow map generation. Notably, the RF model exhibited improved consistency with MODIS reference data, showcasing advancements over traditional methods like the Grody and Basist's algorithm (1996). Moreover, when comparing RF-SCA, PMW-SCA, and MODIS-SCA with station-measured snow depth data, RF-SCA demonstrated slightly higher accuracy, emphasizing its value in overcoming challenges posed by cloud cover in MODIS data. The

study's commendable attempt to enhance snow mapping based on Tb data is underscored by the results of sensitivity tests and importance ranking of input parameters, indicating a realistic relationship learned by the ML model in a data-driven approach. This suggests that ML for snow monitoring based on brightness temperature is not only feasible but can yield superior results with the inclusion of more data.

In Xiao et al.'s (2021) research, the accuracy in forested areas was notably low due to the vegetation effect, a result similarly observed in this study. The RF-SCA exhibited marginal improvement in densely forested alpine regions compared to PMW-SCA, and most underestimated points were attributed to precipitation. Aligning with Tsutsui and Koike's findings in 2012, the overestimation of PMW-SCA (‘POM’) was attributed to the frozen ground effect at low altitudes, where the dielectric properties of frozen soil resemble those of dry snow. In this context, RF-SCA demonstrated significant improvement in those regions, particularly owing to the lower frequency contributions. Comparing with traditional methods that blend snow maps from different sources, the commonality lies in overcoming individual dataset limitations and enhancing overall accuracy, ensuring robust performance under diverse weather conditions. However, the distinct advantage of employing a ML model becomes evident. ML models adept at learning intricate relationships between microwave signatures and optical features, enable enhanced discrimination of snow cover under varying conditions. The integration of both datasets empowers the model to capture the spatial and temporal dynamics of snow cover comprehensively. ML further allows flexibility in incorporating diverse features and parameters, considering external factors like vegetation cover, and terrain conditions, making it a more adaptable, resilient, and dynamic tool for snow monitoring. In contrast to previous studies that used Tb differences as input variables and overlooked low-frequency bands like 6GHz and 10GHz, this research highlighted the significance of lower frequencies in snow detection. The importance ranking of frequencies revealed their crucial role and incorporating them into the ML model led to improved results. This emphasizes the innovation and effectiveness of considering a broader range of frequencies in microwave data for more accurate snow cover estimation.

6.3 Recommendation

The performance of the ML model yielded satisfactory but not entirely optimal results. To further refine the accuracy of binary snow monitoring using ML, it is imperative to incorporate additional snow-related parameters, including topographic data, into the model. A critical consideration involves adjusting the thresholds for NDSI and CPC in MODIS data based on diverse terrains and seasonal variations. The robustness of the trained model can be rigorously tested by evaluating its performance on unseen datasets from Nov, Jan, and Mar, thereby assessing its capability for snow detection across different seasonal conditions. Furthermore, a comprehensive assessment can be achieved by comparing the model's outputs with ground measurement products, such as GlobSnow (https://www.globsnow.info/), providing valuable insights into the model's real-world applicability. Embarking on an exploration of deep learning (DL) techniques, particularly leveraging Convolutional Neural Networks (CNNs), represents a promising avenue for enhancing model training. CNNs, renowned for their capacity to analyze surrounding pixels and discern spatial patterns and latent features within data, offer a potent means to improve classification accuracy and uncover more intricate patterns. This multifaceted approach underscores a commitment to comprehensive model enhancement, contributing significantly to the advancement of ML in the domain of binary snow monitoring.

6.4 Conclusion

In conclusion, this research establishes a crucial foundation for advancing the field of ML in the development of automatic snow classification algorithms utilizing remote sensing data. By demonstrating the effectiveness of merging multiple remote sensing datasets, the study not only enhances the accuracy of snow mapping but also underscores the potential for future algorithmic refinement. The comprehensive integration of diverse datasets, such as PMW Tb and MODIS binary snow data, provides a comprehensive understanding of snow cover dynamics. This approach combining different sensor modalities and leveraging their unique strengths, opens avenues for more sophisticated ML/DL models capable of discerning intricate snow characteristics across various landscapes and environmental conditions. The

findings contribute significantly to the ongoing efforts in advancing remote sensing methodologies for snow monitoring, offering valuable insights for researchers and practitioners working on automated snow classification algorithms. The knowledge gained from this work lays the groundwork for the continued evolution of snow mapping techniques, aligning with the broader goal of enhancing our ability to monitor and understand snow cover on a global scale.

References

Abram, N., J.-P. Gattuso, A. Prakash, L. Cheng, M.P. Chidichimo, S. Crate, H. Enomoto, M. Garschagen, N. Gruber, S. Harper, E. Holland, R.M. Kudela, J. Rice, K. Steffen, K. von Schuckmann, (2019). Framing and Context of the Report. In: IPCC Special Report on the Ocean and Cryosphere in a Changing Climate [H.-O. Pörtner, D.C. Roberts, V. Masson-Delmotte, P. Zhai, M. Tignor, E. Poloczanska, K. Mintenbeck, A. Alegría, M. Nicolai, A. Okem, J. Petzold, B. Rama, N.M. Weyer (eds.)]. Cambridge University Press, Cambridge, UK and New York, NY, USA, pp. 73-129. https://doi.org/10.1017/9781009157964.003.

Armstrong, R. L., Chang, A., Rango, A., et al. (1993). Snow depths and grain-size relationships with relevance for PMW studies. Annals of Glaciology, 17(1), 171-176.

Armstrong, R., Brodzik, M. (1995). An Earth-gridded SSM/I data set for cryospheric studies and global change monitoring. Advances in Space Research, 16(10), 155-163.

Barnett, T. P., Adam, J. C., Lettenmaier, D. P. (2005). Potential impacts of a warming climate on water availability in snow-dominated regions. Nature, 438, 303–309.

Baldridge, A. M., Hook, S. J., Grove, C. I., Rivera, G. (2009). The ASTER Spectral Library Version 2.0.

Beniston, M. (2003). Climatic change in mountain regions: a review of possible impacts. Climatic change, 59(1-2), 5-31.

Bergeron, J., Royer, A., Turcotte, R., Roy, A. (2014). Snow cover estimation using blended MODIS and AMSR-E data for improved watershed-scale spring streamflow simulation in Quebec, Canada. Hydrological processes, 28(16), 4626-4639.

Berghuijs, W., Woods, R., Hrachowitz, M. (2014). A precipitation shift from snow towards rain leads to a decrease in streamflow. Nat. Clim. Change, 4, 583–586.

Brown, R. D., Brasnett, B. R. (2011). The Canadian Meteorological Centre global daily snow depth analysis, 1998–2011: Overview, experience, and applications. In Proc. 68th Eastern Snow Conf (pp. 197-200).

Brown, R. D. and B. Brasnett (2010). Canadian Meteorological Centre (CMC) Daily Snow Depth Analysis Data, Version 1. [Indicate subset used]. Boulder, Colorado USA. NASA National Snow and Ice Data Center Distributed Active Archive Center. https://doi.org/10.5067/W9FOYWH0EQZ3.

Callaghan, T. V., Johansson, M., Key, J., Prowse, T., Ananicheva, M., & Klepikov, A. (2011a). Feedbacks and interactions: From the Arctic cryosphere to the climate system. AMBIO: A Journal of the Human Environment, 40, 75-86

Chang, A., Foster, J., Hall, D. (1987). Nimbus-7 SMMR derived global snow cover parameters. Annals of Glaciology, 9(9), 39-44.

Chang, A., Foster, J., Hall, D., et al. (1997). Snow parameters derived from microwave measurements during the BOREAS winter field campaign. Journal of Geophysical Research: Atmospheres, 102(D24), 29,663-29,671.

Cherkassky, V., & Ma, Y. (2004). Practical selection of SVM parameters and noise estimation for SVM regression. Neural networks, 17(1), 113-126.

Chen, R., Sui, L., Xia, M., & Cao, J. (2023). iEEG Signal Data Augmentation in Convolutional Neural Networks for Epileptic Focus Localization. INTERNATIONAL JOURNAL OF COMPUTERS & TECHNOLOGY, 23, 80–92. https://doi.org/10.24297/ijct.v23i.9482.

Cohen, J. L., Furtado, J. C., Barlow, M. A., Alexeev, V. A., & Cherry, J. E. (2012). Arctic warming, increasing snow cover and widespread boreal winter cooling. Environmental Research Letters, 7, 014007

Chutia, D., Bhattacharyy Fauvel, D. K., Sarma, K. K., Kalita, R., & Sudhakar, S. (2016). Hyperspectral remote sensing classifications: a perspective survey. Transactions in GIS, 20(4), 463-490.

Da Ronco, P., Avanzi, F., De Michele, C., Notarnicola, C., & Schaefli, B. (2020). Comparing MODIS snow products Collection 5 with Collection 6 over Italian Central Apennines. International journal of remote sensing, 41(11), 4174-4205.

Derksen, C., Smith, S. L., Sharp, M., Brown, L., Howell, S., Copland, L., Mueller, D.R., Gauthier, Y., Fletcher, C.G., Tivy, A., Bernier, M., Bourgeois, J., Brown, R.,Burn, C.R., Duguay, C., Kushner, P., Langlois, A., Lewkowicz, A.G., Royer, A. & Walker, A. (2012). Variability and change in the Canadian cryosphere. Climatic Change, 115, 59-88

Ding, Y., Zhang, S., Chen, R. (2020). Cryospheric Hydrology: decode the Largest Freshwater Reservoir on Earth. Bulletin of Chinese Academy of Sciences, 35(4), 414-424.

Ding, Y., Zhang, S., Chen, R., Han, T., Han, H., Wu, J., ... & Chang, Y. (2020). Hydrological basis and discipline system of cryohydrology: From a perspective of cryospheric science. Frontiers in Earth Science, 8, 566.

Dobos, E. (2020). Albedo. In Atmosphere and Climate (pp. 25-28). CRC Press.

England A W. Thermal microwave emission from a scattering layer. Journal of Geophysical Research, 1975, 80(32), 4484-4496.

Fletcher CG, Zhao H, Kushner PJ, et al. (2012). Using models and satellite observations to evaluate the strength of snow albedo feedback. Journal of Geophysical Research, 117(D11), D11117. Available from: http://doi.wiley.com.proxy.lib.uwaterloo.ca/10.1029/2012JD017724.

Foster, J. L., Hall, D. K., Chang, A. T. C., & Rango, A. (1984). An overview of passive microwave snow research and results. Reviews of Geophysics, 22(2), 195-208.

Foster, J., Chang, A., Hall, D. (1997). Comparison of snow mass estimates from a prototype passive microwave snow algorithm, a revised algorithm, and a snow depth climatology. Remote Sensing of Environment, 62(2), 132-142.

Foster, J. L., Hall, D. K., Eylander, J. B., Riggs, G. A., Nghiem, S. V., Tedesco, M., ... & Choudhury, B. (2011). A blended global snow product using visible, PMW, and scatterometer satellite data. International journal of remote sensing, 32(5), 1371-1395.

Gascoin, S., M. Grizonnet, M. Bouchet, G. Salgues, and O. Hagolle. 2019. "Theia Snow Collection: High-resolution Operational Snow Cover Maps from Sentinel-2 and Landsat-8 Data." Earth Syst Sci Data, 11(2), 493–514.

Gascoin, S., Z. Barrou Dumont, C. Deschamps-Berger, F. Marti, G. Salgues, J. I. López-Moreno, J. Revuelto, T. Michon, P. Schattan, and O. Hagolle. 2020. "Estimating Fractional Snow Cover in Open Terrain from Sentinel-2 Using the Normalized Difference Snow Index." Remote Sensing, 12(18), 2904. https://www.mdpi.com/2072-4292/12/18/2904.

Gharaei-Manesh S, Fathzadeh A, Taghizadeh-Mehrjardi R. Comparison of artificial neural network and decision tree models in estimating spatial distribution of snow depth in a semi-arid region of Iran. Cold Regions Science & Technology, 2016, 122, 26-35.

Giddings, J. C., & LaChapelle, E. (1962). The formation rate of depth hoar. Journal of Geophysical Research, 67(6), 2377-2383.

Grody, N.C.; Basist, A.N. Global identification of snowcover using SSM/I measurements. IEEE Trans. Geosci. Remote Sens. 1996, 34, 237–249.

Hallikainen M T, Ulaby F T, Van Deventer T E. Extinction behavior of dry snow in the 18-to 90-GHz range. IEEE Transactions on Geoscience and Remote Sensing, 1987, 25(6), 737-745.

Hall, D. K., Chang, A. T. C., & Foster, J. L. (1986). Detection of the depth-hoar layer in the snow-pack of the Arctic coastal plain of Alaska, USA, using satellite data. Journal of Glaciology, 32(110), 87-94.

Hall, D.K.; Kelly, R.E.; Riggs, G.A.; Chang, A.T.; Foster, J.L. Assessment of the relative accuracy of hemispheric-scale snow-cover maps. Ann. Glaciol., 2002, 34, 24–30.

HALL D K, RIGGS G A, SALOMONSON V V, et al. MODIS Snow-Cover Products. Remote Sensing of Environment, 2002, 83 (1-2), 181–194. DOI:10.1016/S0034-4257(02)00095-0.

Hall, D.K.; Riggs, G.A. Accuracy assessment of the MODIS snow products. Hydrol. Process., 2007, 21, 1534–1547.

Hall, D. K., Riggs, G. A., DiGirolamo, N. E., & Román, M. O. (2019). MODIS cloud-gap filled snow-cover products: Advantages and uncertainties. Hydrol. Earth Syst. Sci. Discuss, 123, 1-23.

Hall, D. K. and G. A. Riggs. 2020. MODIS/Terra CGF Snow Cover Daily L3 Global 500m SIN Grid, Version 61. Boulder, Colorado USA. NASA National Snow and Ice Data Center Distributed Active Archive Center. https://doi.org/10.5067/MODIS/MOD10A1F.061.

Hernández-Henríquez MA, Déry SJ, Derksen C (2015). Polar amplification and elevation-dependence in trends of Northern Hemisphere snow cover extent, 1971–2014. Environmental Research Letters, 10(4), 044010. Available from: http://stacks.iop.org.proxy.lib.uwaterloo.ca/1748-9326/10/i=4/a=044010?key=crossref.b55e798eb3b71ed93a470e90538c4c67.

Hofer R, Mätzler C. Investigations on snow parameters by radiometry in the 3-to 60-mm wavelength region. Journal of Geophysical Research: Oceans, 1980, 85(C1), 453-460.

Hosmer Jr, D. W., Lemeshow, S., & Sturdivant, R. X. (2013). Applied logistic regression (Vol. 398). John Wiley & Sons.

Joachims, T. (1999). Svmlight: Support vector machine. SVM-Light Support Vector Machine. http://svmlight.joachims.org/, University of Dortmund, 19(4), 25.

IPCC (2021). Climate Change 2021: The Physical Science Basis. Contribution of Working Group I to the Sixth Assessment Report of the Intergovernmental Panel on Climate Change [Masson-Delmotte, V., P. Zhai, A. Pirani, S.L. Connors, C. Péan, S. Berger, N. Caud, Y. Chen, L. Goldfarb, M.I. Gomis, M. Huang, K. Leitzell, E. Lonnoy, J.B.R. Matthews, T.K. Maycock, T. Waterfield, O. Yelekçi, R. Yu, and B. Zhou (eds.)]. Cambridge University Press, Cambridge, United Kingdom and New York, NY, USA, 2391 pp. doi:10.1017/9781009157896.

Karaca, Baleanu, D. (Dumitru), Zhang, Y.-D., Gervasi, O., & Moonis, M. (Eds.). (2022). Multi-chaos, fractal, and multi-fractional artificial intelligence of different complex systems. Academic Press.

Kelly, R. E., Chang, A. T., Tsang, L., & Foster, J. L. (2003). A prototype AMSR-E global snow area and snow depth algorithm. IEEE Transactions on Geoscience and Remote Sensing, 41(2), 230-242.

Kelly, R. (2009). The AMSR-E snow depth algorithm: Description and initial results. Journal of the Remote Sensing Society of Japan, 29(1), 307-317.

Klein A, Barnett AC. 2003. Validation of daily MODIS snow maps of the Upper Rio Grande River Basin for the 2000-2001 snow year. Remote Sensing of Environment 86: 162–176.

Kinar, N. J., and J. W. Pomeroy. 2015. “Measurement of the Physical Properties of the Snowpack.” Rev Geophys 53 (2): 481–544.

Kunzi, K. F., S. Patil, and H. Rott. 1982. “Snow-Cover Parameters Retrieved from Nimbus-7 Scanning Multichannel Microwave Radiometer (SMMR) Data.” IEEE Transactions on Geoscience and Remote Sensing : A Publication of the IEEE Geoscience and Remote Sensing Society, GE-20 (4), 452–467.

Kwon, Y., Forman, B. A., Ahmad, J. A., Kumar, S. V., & Yoon, Y. (2019). Exploring the utility of ML-based PMW Tb data assimilation over terrestrial snow in high mountain Asia. Remote Sensing, 11(19), 2265.

Lehner, B., & Döll, P. (2004). Development and validation of a global database of lakes, reservoirs, and wetlands. Journal of hydrology, 296(1-4), 1-22.

Liang, J., Liu, X., Huang, K., Li, X., Shi, X., Chen, Y., & Li, J. (2015). Improved snow depth retrieval by integrating microwave Tb and visible/infrared reflectance. Remote Sensing of Environment, 156, 500-509.

Liashchynskyi, P., & Liashchynskyi, P. (2019). Grid search, random search, genetic algorithm: a big comparison for NAS. arXiv preprint arXiv:1912.06059.

Luo, J., Dong, C., Lin, K., Chen, X., Zhao, L., & Menzel, L. (2022). Mapping snow cover in forests using optical remote sensing, ML, and time-lapse photography. Remote Sensing of Environment, 275, 113017.

Masson-Delmotte V, Kageyama M, Braconnot P, et al. Past and future polar amplification of climate change: climate model intercomparisons and ice-core constraints. Climate Dynamics, 2006, 26(5), 513–529.

Musa, A. B. (2013). Comparative study on classification performance between support vector machine and logistic regression. International Journal of Machine Learning and Cybernetics, 4(1), 13–24. https://doi.org/10.1007/s13042-012-0068-x

Pavlov, Y. L. (2000). RFs. Vsp.

Pepe, M., P. A. Brivio, A. Rampini, F. R. Nodari, and M. Boschetti. 2005. “Snow Cover Monitoring in Alpine Regions Using ENVISAT Optical Data.” International Journal of Remote Sensing, 26 (21), 4661–4667.

Picard, G., Sandells, M., & Löwe, H. (2018). SMRT: An active–passive microwave radiative transfer model for snow with multiple microstructure and scattering formulations (v1. 0). Geoscientific Model Development, 11(7), 2763-2788.

Poussin, C., Timoner, P., Chatenoux, B., Giuliani, G., & Peduzzi, P. (2023). Improved Landsat-based snow cover mapping accuracy using a spatiotemporal NDSI and generalized linear mixed model. Science of Remote Sensing, 7, 100078.

Pulliainen J T,Grandell J,Hallikainen M T. HUT snow emission model and its applicability to snow water equivalent retrieval. IEEE Transactions on Geoscience and Remote Sensing,1999,37 (3), 1378-1390.

Riggs, G.A., Hall D.K., Román M.O. MODIS snow products user guide for Collection 6 (2016).

Screen, J. A., & Simmonds, I. (2010). The central role of diminishing sea ice in recent Arctic temperature amplification. Nature, 464(7293), 1334-1337.

Sheykhmousa, M., Mahdianpari, M., Ghanbari, H., Mohammadimanesh, F., Ghamisi, P., & Homayouni, S. (2020). Support vector machine versus RF for remote sensing image classification: A meta-analysis and systematic review. IEEE Journal of Selected Topics in Applied Earth Observations and Remote Sensing, 13, 6308-6325.

Shi, J., S. Hensley, and J. Dozier. 2000. "Mapping Snow with Repeat Pass Synthetic Aperture Radar." Geosci Remote Sensing, 1997 IGARSS '97 Remote Sens - A Sci Vis Sustain Dev 1997 IEEE Int, 2000 (267), 339–342.

Shi X, Marsh P, Yang D. Warming spring air temperatures, but delayed spring streamflow in an Arctic headwater basin. Environmental Research Letters, 2015, 10(6), 064003.

Sharma, R. C., R. Tateishi, and K. Hara. 2016. "A New Water-resistant Snow Index for the Detection and Mapping of Snow Cover on A Global Scale." International Journal of Remote Sensing, 37 (11), 2706–2723.

Shi, J.C.; Xiong, C.; Jiang, L.M. Review of snow water equivalent microwave remote sensing. Sci. China Earth Sci., 2016, 59, 731–745.

Singh, G., G. Venkataraman, Y. S. Rao, V. Kumar, and Snehmani. 2008. "The H/A/ALPHA Polarimetric decomposition Theorem and Complex Wishart Distribution for Snow

Cover Monitoring." International Geoscience and Remote Sensing Symposium, 4, IV–1081.

Sun, Z., & Shi, J. (2006). Development of snow depth and snow water equivalent algorithm in Western China using passive microwave remote sensing data. *Advances in earth science*, *21*(12), 1363.

Sun, Z.W.; Yu, P.S.; Xia, L.; Wu, S.L.; Jiang, L.M.; Guo, L. Progress in study of snow parameter inversion by passive microwave remote sensing. Remote Sens. Land Resour. 2015, 27, 9–15. (In Chinese)

Strozzi, T., U. Wegmuller, and C. Matzler. 1999. "Mapping Wet Snowcovers with SAR Interferometry." International Journal of Remote Sensing, 20 (12), 2621–2631.

Sturm, M., Holmgren, J., & Liston, G. E. (1995). A seasonal snow cover classification system for local to global applications. Journal of Climate, 8(5), 1261-1283.

Sturm, M., Goldstein, M. A., & Parr, C. (2017). Water and life from snow: A trillion dollar science question. Water Resources Research, 53(5), 3534-3544.

Sturm, M., & Holmgren, J. (2018). An automatic snow depth probe for field validation campaigns. Water Resources Research, 54(11), 9695-9701.

Sturm, M., & Liston, G. E. (2021). Revisiting the global seasonal snow classification: An updated dataset for earth system applications. Journal of Hydrometeorology, 22(11), 2917-2938.

Thackeray, C. W., Fletcher, C. G., Mudryk, L. R., & Derksen, C. (2016). Quantifying the uncertainty in historical and future simulations of Northern Hemisphere spring snow cover. Journal of Climate, 29(23), 8647-8663.

Thackeray, C. W., Derksen, C., Fletcher, C. G., & Hall, A. (2019). Snow and climate: Feedbacks, drivers, and indices of change. Current Climate Change Reports, 5, 322-333.

Tong, J., Dery, S. J., Jackson, P. L., & Derksen, C. (2010). Testing snow water equivalent retrieval algorithms for passive microwave remote sensing in an alpine watershed of western Canada. Canadian Journal of Remote Sensing, 36(sup1), S74-S86.

Tsutsui, H., & Koike, T. (2012). Development of snow retrieval algorithm using AMSR-E for the BJ ground-based station on seasonally frozen ground at low altitude on the Tibetan Plateau. 気象集誌. 第 2 輯, 90(0), 99-112.

Ulaby, F. T., Moore, R. K., & Fung, A. K. (1981). Microwave remote sensing: Active and passive. volume 1-microwave remote sensing fundamentals and radiometry.

Vander Jagt, B. J., Durand, M. T., Margulis, S. A., Kim, E. J., & Molotch, N. P. (2013). The effect of spatial variability on the sensitivity of passive microwave measurements to snow water equivalent. Remote sensing of environment, 136, 163-179.

Wei, Y., Li, X., Li, L., Gu, L., Zheng, X., Jiang, T., & Li, X. (2022). An approach to improve the spatial resolution and accuracy of AMSR2 passive microwave snow depth product using machine learning in Northeast China. Remote Sensing, 14(6), 1480.

Whyte, A., Ferentinos, K. P., & Petropoulos, G. P. (2018). A new synergistic approach for monitoring wetlands using Sentinels-1 and 2 data with object-based machine learning algorithms. Environmental Modelling & Software, 104, 40-54.

Wiesmann, A., & Mätzler, C. (1999). Microwave emission model of layered snowpacks. Remote sensing of environment, 70(3), 307-316.

Xiao, X., Zhang, T., Zhong, X., Shao, W., & Li, X. (2018). Support vector regression snow-depth retrieval algorithm using passive microwave remote sensing data. Remote sensing of environment, 210, 48-64.

Xiao, X., Liang, S., He, T., Wu, D., Pei, C., & Gong, J. (2021). Estimating fractional snow cover from passive microwave brightness temperature data using MODIS snow cover product over North America. The Cryosphere, 15(2), 835-861.

Xue, Y., & Forman, B. A. (2015). Comparison of passive microwave brightness temperature prediction sensitivities over snow-covered land in North America using machine learning algorithms and the Advanced Microwave Scanning Radiometer. Remote Sensing of Environment, 170, 153-165.

Zhang, H., Zhang, F., Zhang, G., Che, T., Yan, W., Ye, M., & Ma, N. (2019). Ground-based evaluation of MODIS snow cover product V6 across China: Implications for the selection of NDSI threshold. Science of the Total Environment, 651, 2712-2726.

Zschenderlein, L., Luojus, K., Takala, M., Venäläinen, P., & Pulliainen, J. (2023). Evaluation of passive microwave dry snow detection algorithms and application to SWE retrieval during seasonal snow accumulation. Remote Sensing of Environment, 288, 113476.